

TOPICAL REVIEW • OPEN ACCESS

Flexible gallium oxide electronics

To cite this article: Xiao Tang *et al* 2023 *Semicond. Sci. Technol.* **38** 063001



View the [article online](#) for updates and enhancements.

You may also like

- [A state-of-art review on gallium oxide field-effect transistors](#)
Rundi Qiao, Hongpeng Zhang, Shuting Zhao et al.
- [Review of polymorphous Ga₂O₃ materials and their solar-blind photodetector applications](#)
Xiaohu Hou, Yanni Zou, Mengfan Ding et al.
- [Review of deep ultraviolet photodetector based on gallium oxide](#)
Yuan Qin, , Shibing Long et al.

Topical Review

Flexible gallium oxide electronics

Xiao Tang , Yi Lu and Xiaohang Li* 

Advanced Semiconductor Laboratory, King Abdullah University of Science and Technology (KAUST), Thuwal 23955-6900, Saudi Arabia

E-mail: xiaohang.li@kaust.edu.sa

Received 28 December 2022, revised 28 February 2023

Accepted for publication 5 April 2023

Published 20 April 2023



CrossMark

Abstract

Flexible Ga₂O₃ devices are becoming increasingly important in the world of electronic products due to their unique properties. As a semiconductor, Ga₂O₃ has a much higher bandgap, breakdown electric field, and dielectric constant than silicon, making it a great choice for next-generation semiconductor materials. In addition, Ga₂O₃ is a particularly robust material that can withstand a wide range of temperatures and pressure levels, thus is ideal for harsh environments such as space or extreme temperatures. Finally, its superior electron transport properties enable higher levels of electrical switching speed than traditional semiconducting materials. Endowing Ga₂O₃-based devices with good mechanical robustness and flexibility is crucial to make them suitable for use in applications such as wearable electronics, implantable electronics, and automotive electronics. However, as a typical ceramic material, Ga₂O₃ is intrinsically brittle and requires high temperatures for its crystallization. Therefore fabricating flexible Ga₂O₃ devices is not a straightforward task by directly utilizing the commonly used polymer substrates. In this context, in recent years people have developed several fabrication routes, which are the transfer route, *in situ* room-temperature amorphous route, and *in situ* high-temperature epitaxy route. In this review, we discuss the advantages and limitations of each technique and evaluate the opportunities for and challenges in realizing the applications of flexible Ga₂O₃ devices.

Keywords: flexible, gallium oxide, electronics

(Some figures may appear in colour only in the online journal)

1. Introduction

In the last decade, gallium oxide (Ga₂O₃) materials and devices have garnered immense interest owing to their unique properties, such as wide bandgap (4.9 eV), high breakdown electric fields ($E_{br} = 8 \text{ MV cm}^{-1}$), and thermal stability [1–10]. Compared with SiC (317.1) and GaN (846.0),

Ga₂O₃ has an exceptionally high Baliga figure of merit of 3214.1, making it a promising candidate for various applications, including power electronics, solar-blind ultraviolet (UV) detectors, memory devices, and electronics that operate under harsh environments such as high temperature and radiation [11–18].

In addition, various electronics that have been developed in the past decade have become indispensable in our daily lives. Hence, there is considerable interest in developing portable and wearable electronics for real-time applications. Mechanically flexible electronic systems must be designed to withstand applied bending stress caused by curvilinear surfaces and movements [19–24]. The application of flexible electronics is depicted in figure 1. Organic or low-temperature-processed

* Author to whom any correspondence should be addressed.



Original content from this work may be used under the terms of the [Creative Commons Attribution 4.0 licence](https://creativecommons.org/licenses/by/4.0/). Any further distribution of this work must maintain attribution to the author(s) and the title of the work, journal citation and DOI.

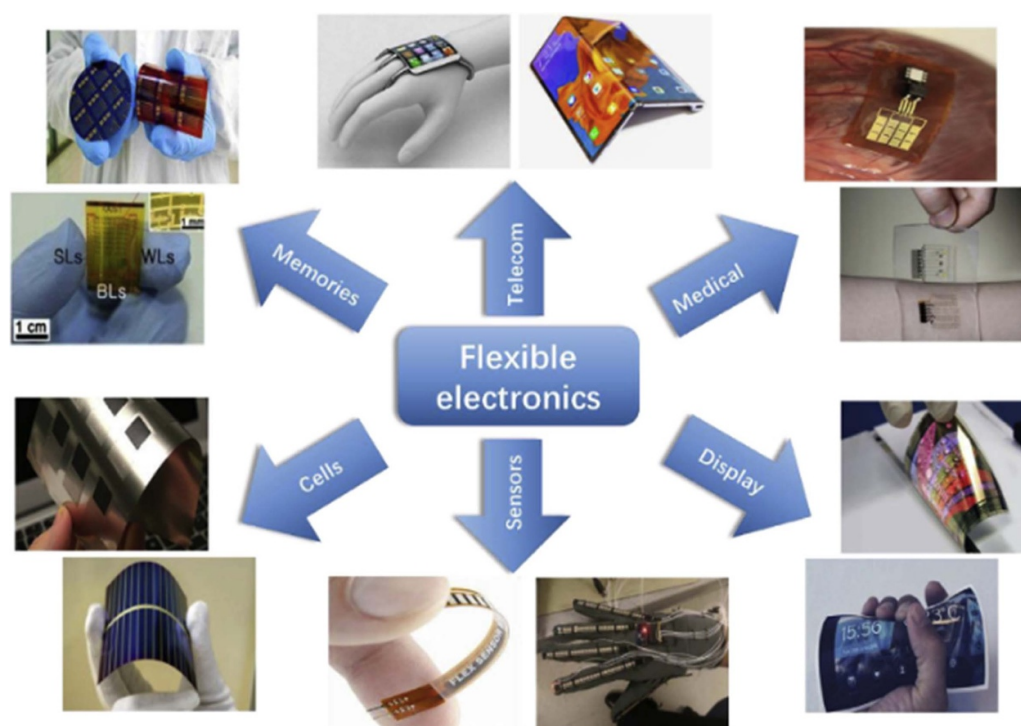


Figure 1. Typical flexible electronics and their applications [19]. Copyright 2020 Elsevier.

inorganic flexible semiconductor electronics have been extensively investigated [25–28]. Alternatively, the growth of oxide ceramic semiconductor materials usually requires high-temperature processing and epitaxial templates [29–31]. In addition, owing to the lack of suitable flexible substrates, the integration of these high-temperature-processed materials into flexible electronics remains challenging. Ga_2O_3 is a typical representative of oxide semiconductor materials [1]. For instance, Ga_2O_3 has five polymorphs: α , β , γ , δ , and ϵ . [32, 33] Among them, β - Ga_2O_3 has the highest thermal stability [1, 32]. However, the crystallization temperature of β - Ga_2O_3 is 1000 °C, at least for solid reactions under normal pressure, which is considerably higher than the decomposition temperatures of conventional organic flexible substrates (usually 200 °C–300 °C) [1, 34]. Accordingly, the selection of the substrate, deposition technique, and Ga_2O_3 polymorph is critical. The fabrication of Ga_2O_3 has been extensively studied for flexible electronics recently [35, 36]. In this review, we highlight key developments in Ga_2O_3 flexible electronics and predict the direction of their future applications.

2. Crystal structure and deposition techniques

A detailed understanding of the polymorphs and the corresponding deposition techniques of Ga_2O_3 is essential for designing an appropriate fabrication process for flexible electronics. Ga_2O_3 has mainly five polymorphs, i.e. α - Ga_2O_3 (trigonal (R3-c) corundum structure), β - Ga_2O_3 (monoclinic (C2/m)), γ - Ga_2O_3 (cubic (Fd3-m) spinel structure), δ - Ga_2O_3 (orthorhombic system (Cmcm)), and ϵ - Ga_2O_3 (hexagonal system (Pna21)). The structural information and unit cells

Table 1. Summary of the structures of Ga_2O_3 polymorphs [3, 33, 37–39].

Polymorph of Ga_2O_3	Structure	Space group	Lattice parameters
α	Rhombohedral	R-3 c	$a = 4.9825 \text{ \AA}$, $c = 13.433 \text{ \AA}$
β	Monoclinic	C2/m	$a = 12.23 \text{ \AA}$, $b = 3.04 \text{ \AA}$, $c = 5.80 \text{ \AA}$
γ	Cubic	Fd-3 m	$a = b = c = 8.45 \text{ \AA}$
δ	Body-centered cube	La3	$a = 9.401$
ϵ	Orthorhombic	Pna21	$a = 5.046 \text{ \AA}$, $b = 8.634 \text{ \AA}$, $c = 9.209 \text{ \AA}$

of its polymorphs are provided in table 1 and figure 2, respectively [3, 33, 37–40]. Other than these crystalized structures, amorphous Ga_2O_3 also plays an important role in flexible electronics as it does not require high temperatures for deposition [41–43].

Specifically, α - Ga_2O_3 is a crystallized metastable phase that can be obtained at very low temperatures. α - Ga_2O_3 thin films can be obtained through mist chemical vapor deposition (mist-CVD), [44–46] which is facile and cost-effective and does not require vacuum equipment. In addition, it allows the tailoring of the deposition precursor solution. Using aqueous halide solutions, gallium salts can be easily mixed with indium and aluminum to obtain corundum-structured III-oxide alloys with various stoichiometries, offering bandgap engineering from 3.8 eV to 8.8 eV [3, 47]. Further, α - Ga_2O_3 can be

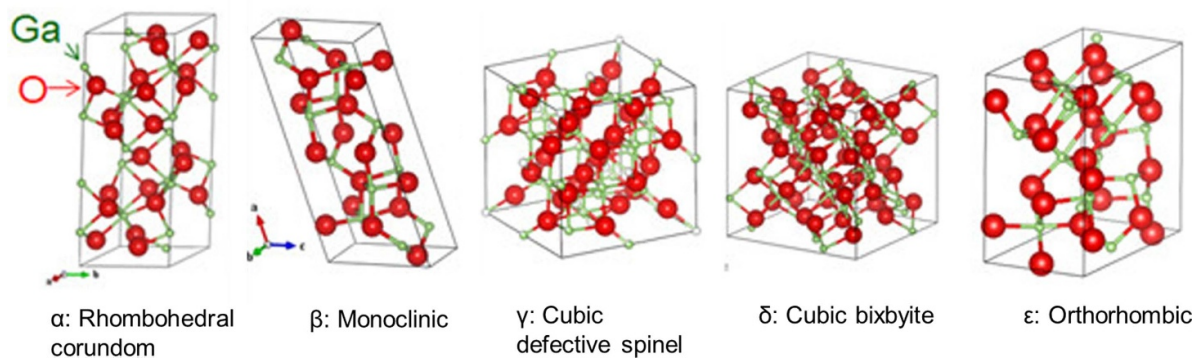


Figure 2. Polymorphs of Ga_2O_3 [40]. Copyright 2022 AIP.

obtained by simply heating GaOOH using the hydrothermal method and halide vapor phase epitaxy (HVPE) [48, 49]. However, the hydrothermal route is difficult to scale up, whereas the HVPE route requires highly corrosive HCl gas as the precursor and is relatively more expensive compared to mist-CVD.

Owing to its cubic spinel structure, $\gamma\text{-Ga}_2\text{O}_3$ shows ferromagnetism at room temperature when doped with manganese, making it a promising spintronic material [50, 51]. The common deposition techniques for $\gamma\text{-Ga}_2\text{O}_3$ are molecular beam epitaxy (MBE) and pulsed laser deposition (PLD) [37, 52].

$\epsilon\text{-Ga}_2\text{O}_3$ has a hexagonal structure exhibiting a large spontaneous polarization [21]. Hence, it is a promising conducting channel material in heterostructure field-effect transistors because it can produce high-density two-dimensional electron gas [53]. $\epsilon\text{-Ga}_2\text{O}_3$ thin films have been grown using HVPE, plasma-assisted MBE, and metal–organic CVD (MOCVD) [54–56]. Notably, although $k\text{-Ga}_2\text{O}_3$ has an orthorhombic phase, it has been widely confused with $\epsilon\text{-Ga}_2\text{O}_3$ [1].

Owing to its highest thermal stability among the polymorphs, monoclinic $\beta\text{-Ga}_2\text{O}_3$ has been extensively investigated [1, 3, 35, 57]. It has a wide bandgap (4.9 eV), high breakdown electric fields theoretically reaching $E_{\text{br}} = 8 \text{ MV cm}^{-1}$, and a three-times higher Baliga figure of merit compared with GaN ; thus, it can be widely used in DUV photodetectors (PDs), thin film transistors (TFTs), and Schottky barrier diodes (SBDs) [1, 57, 58]. $\beta\text{-Ga}_2\text{O}_3$ can be grown using common deposition techniques, such as sol–gel, PLD, MOCVD, and MBE [59–62]. Moreover, as the most stable phase among the polymorphs, $\beta\text{-Ga}_2\text{O}_3$ can be converted from the other isomers upon high-temperature sintering. The transition of the other isomers to the $\beta\text{-Ga}_2\text{O}_3$ phase is depicted in figure 3 [32].

Finally, amorphous Ga_2O_3 has a large number of defects and oxygen vacancies compared with its crystalline counterparts, thus making its use in electronic devices disadvantageous because of its relatively slow photoelectric response and unstable performance over time [1, 3, 63]. Amorphous Ga_2O_3 thin films can be deposited on polymer substrates via sputtering at room temperature, which can be valuable for fabricating flexible electronics [64]. In addition, the aforementioned

inferior properties of amorphous Ga_2O_3 can be improved by subsequent processes after film deposition [64].

3. Flexible substrates

The primary property of flexible substrates is deformability, which allows coated electronics to withstand bending and twisting when placed in pockets or directly attached to the body. Further more, the good mechanical performance of flexible substrates can enable the large-scale production of electronics in a continuous reel-to-reel system, thereby decreasing the production cost [65–67]. In general, three types of materials, polymers, glass fibers, and metal foils, can meet these mechanical requirements, the main properties of which are summarized in table 2 [68–72].

Polymer substrates are highly flexible, cost effective, transparent, and suitable for continuous reel-to-reel fabrication systems. So far, widely used polymer substrates include polyimide (PI), polyether sulfone, polyetherimide, and polyethylene naphthalate (PEN) [73–76]. However, polymer substrates suffer from low decomposition or glass transition temperatures. [72] Few materials, such as carbon nanotubes, transition metal dichalcogenides, organic compounds, and perovskites, have been grown on polymers because they require neither high processing temperature ($>300^\circ\text{C}$) nor high crystallinity (in terms of grain size and orientation) [26, 77, 78]. Moreover, the elastic moduli of polymer substrates are significantly smaller than those of ceramic semiconductor materials, and thermal mismatch can cause shattering and falloff during fabrication [72].

Compared with polymers, glass has higher thermal stability and can withstand elevated temperatures (up to 1200°C) [72]. Usually, flexible glass substrates can be obtained by thinning a thick rigid glass plate to hundreds of microns using a down draw method. As glass offers electrical resistance and high optical transparency, it has been used as the standard substrate in flexible panel displays. However, despite its high thermal stability, glass cannot serve as an epitaxial template for the growth of epitaxial semiconductor thin films owing to its amorphous nature.

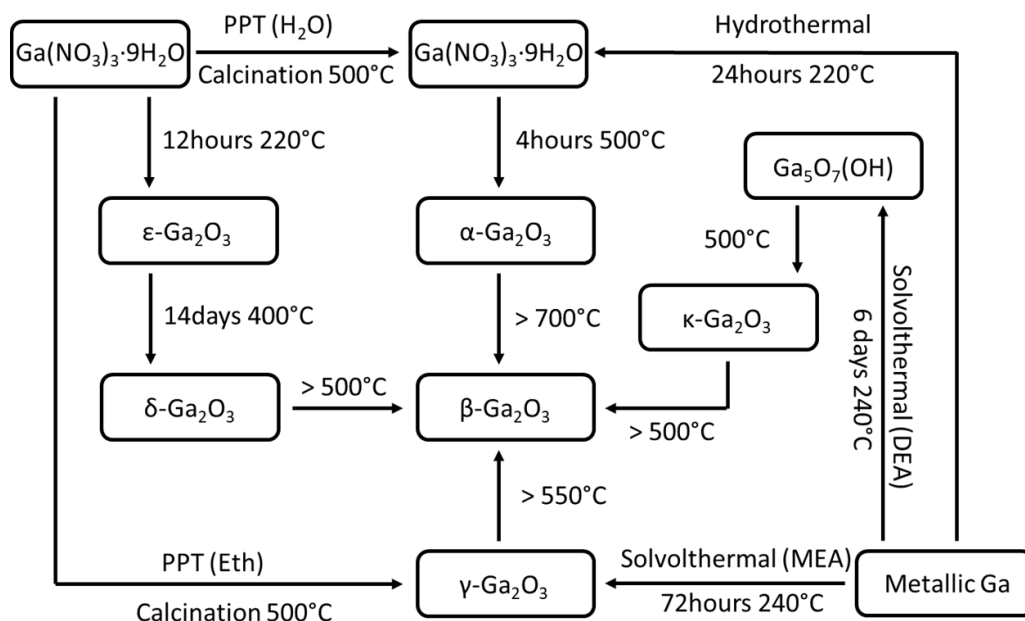


Figure 3. Interconversion of Ga_2O_3 polymorphs (PPT = precipitate, DEA = diethanolamine, and MEA = monoethanolamine) [32]. Copyright 2013 Wiley.

Table 2. Summary of the properties of flexible substrates [68–72].

Type of substrate	Flexibility	Thermal stability	Epitaxial capability
Polymer	Yes	No	No
Glass	Yes	Yes	No
Metal foil	Yes	Yes	No
Muscovite	Yes	Yes	Yes

As another class of flexible substrates, metal foils exhibit good mechanical performance and high thermal stability and do not react with moisture and oxygen; thus, they have been used in flexible reflective display panels and amorphous silicon solar cells [72, 79, 80]. For instance, stainless steel can withstand high temperatures (up to 1300 °C) and is thermally much more stable than polymers and glass [81]. Because of this property, it can be used as a substrate for the growth of ceramic semiconductor thin films [82, 83]. The processing temperature ranges for the representative metal foil and polymer substrates and the required temperatures for the crystallization of representative oxide thin films are shown in figure 4 [35]. The thermal stability of metal foils meets the requirement for the crystallization of oxide thin films. In contrast, metal foils have relatively high roughness [72, 84–86]. Because metal foils are produced by pressing metal ingots and then elongating them in a reel system, the roughness of the product is highly dependent on the smoothness of the reel and the subsequent polishing processes and is rarely <100 nm. Therefore, an additional planarization oxide coating becomes necessary for decreasing roughness before the growth of semiconductor layers, which undoubtedly increases the complexity of the use of metal foils [35, 84]. In contrast, by applying ion-beam-assisted deposition (IBAD), the coated oxide planarization layer can be crystallized along a preferred orientation [87, 88]. This technique allows metal foils to serve as a

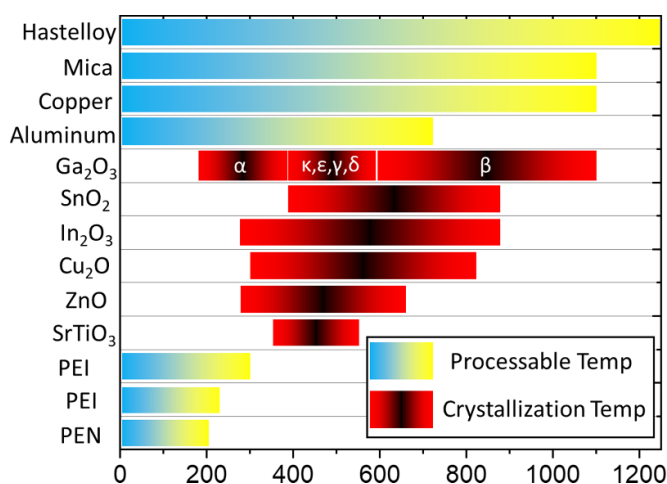


Figure 4. Crystallization temperatures of representative monocrystalline oxide semiconductors and processing temperature ranges of organic and metallic flexible substrates [35]. Copyright 2022 ACS.

high-temperature epitaxial growth template for high-quality semiconductor thin films [35, 82, 89]. So far, the technique has been successfully applied in the coated-conductor industry, especially for the production of superconductor tapes [87, 88].

As a ceramic material crystalized in a monoclinic structure, muscovite (mica) can intrinsically serve as an epitaxial template [36]. Such structure property makes mica sheet ideal for the deposition of crystalized Ga_2O_3 thin films. By thinning to micrometers, the obtained mica sheets can show excellent flexible performances. Moreover, as a typical ceramic material, mica sheets have thermal stability at high temperatures (up to 1600 °C), amazing dielectric strength, chemical inertness, elasticity, lightweight, and refractive properties. Therefore, mica sheets can simultaneously meet the two basic requirements, that is, thermal stability and epitaxial ability, for the direct deposition of flexible crystallized oxide materials.

4. Transfer technique

Monoclinic $\beta\text{-Ga}_2\text{O}_3$ is the most stable polymorph of Ga_2O_3 [1, 33]. However, the growth of high-quality $\beta\text{-Ga}_2\text{O}_3$ requires ideal templates and high temperatures [33, 35]. Thus, it is challenging to grow them directly on conventional flexible polymer substrates. A straightforward strategy to fabricate flexible $\beta\text{-Ga}_2\text{O}_3$ electronics is to use the transfer technique in which bulk single-crystalline $\beta\text{-Ga}_2\text{O}_3$ is first obtained using conventional high-temperature growth routes and $\beta\text{-Ga}_2\text{O}_3$ thin films are then exfoliated from bulk materials and pasted on flexible polymer substrates [90–97]. Single-crystalline $\beta\text{-Ga}_2\text{O}_3$ has been commonly obtained using the Czochralski method, in which Ga_2O_3 powders are melted in an iridium crucible at a temperature of >1820 °C in an oxygen-deficient atmosphere [98]. Upon cooling to room temperature, cylinder bulk $\beta\text{-Ga}_2\text{O}_3$ materials with diameters and lengths of tens of millimeters are obtained. Low-dimensional $\beta\text{-Ga}_2\text{O}_3$ can be directly exfoliated from bulk materials; otherwise, bulk materials can be first used as the homoepitaxial template to grow single-crystalline $\beta\text{-Ga}_2\text{O}_3$ thin films using MBE; then, the thin films serve as the materials for exfoliation [90–97]. Figure 5 depicts the typical exfoliation–transfer procedure, which has been used for the fabrication of various flexible materials, including graphene, black phosphorus, GaN, and MoS_2 [99–102].

First, a scotch tape is used to cleave $\beta\text{-Ga}_2\text{O}_3$ thin layers from the bulk/thin film materials. The layer thickness can be decreased to a nanometer scale by folding and unfolding the scotch tape multiple times. Notably, the acquired layer is usually (100)-oriented because it is the easiest cleavage plane of $\beta\text{-Ga}_2\text{O}_3$. Then, a SiO_2/Si substrate is pasted on the scotch tape after cleaning with acetone and isopropanol. Upon removing the scotch tape, $\beta\text{-Ga}_2\text{O}_3$ layers remain on top of the SiO_2 due to the adhesive force. Then, the SiO_2/Si substrate is cleaned with acetone under ultrasonication, which removes weakly attached $\beta\text{-Ga}_2\text{O}_3$ fragments. Finally, $\beta\text{-Ga}_2\text{O}_3$ thin layers are transferred from the SiO_2/Si substrate to flexible polymer substrates using an elastomeric stamp. Although the transfer technique ensures high-quality materials, it cannot be scaled up owing to uncontrollable and cumbersome manual operation. Thus, to date, the transfer technique has been applied only to basic research [90–97].

Swinnich *et al* [93], Hasan *et al* [95] and Lai *et al* [96] synthesized flexible $\beta\text{-Ga}_2\text{O}_3$ nanomembrane SBDs for applications in high-power electronics using the aforementioned transfer technique [93, 95]. The source single-crystalline Sn-doped $\beta\text{-Ga}_2\text{O}_3$ was obtained via MBE, and the mechanically cleaved fragmental $\beta\text{-Ga}_2\text{O}_3$ layers were transferred to the flexible PI substrates. Because the polymer substrate cannot withstand high temperatures, an inductively coupled plasma treatment was used instead of high-temperature rapid annealing to achieve an ohmic contact between Ti/Au and $\beta\text{-Ga}_2\text{O}_3$, which is important for obtaining high electrical performance [103]. Swinnich *et al* further investigated the influence of bending-induced strain on the electrical performance of flexible devices. The fabricated device and the corresponding electrical performances together with the microstructural images before and after the bending tests are shown in figure 6 [93]. First, using Raman spectroscopy, Swinnich *et al* demonstrated that the exfoliation process did not induce any built-in strain; thus, the high quality of single-crystalline $\beta\text{-Ga}_2\text{O}_3$ can be largely maintained (figure 6(a)). Correspondingly, the flexible SBD exhibited an excellent rectifying behavior similar to $\beta\text{-Ga}_2\text{O}_3$ SBDs with conventional rigid single-crystalline substrates (figure 6(d)). Moreover, the device had a remarkably high breakdown voltage of -119 V, corresponding to a critical breakdown field strength of 1.2 MW cm^{-1} (figure 6(c)). However, the electrical characteristics noticeably degraded under strain, and the forward current and the reverse current were hundreds of times lower when the device was bent (figure 6(d)). The scanning electron microscopy (SEM) images obtained using the initial flat SBD showed a smooth surface, whereas the samples after bending showed fractured surfaces with noticeable microcracks (figures 6(e) and (f)). These microcracks caused the degradation of the current by creating voids and defects, which could lengthen the shortest path of electrons from one end to the other. Hasan *et al* reported another reason for electrical performance degradation, i.e. the generation of nanogaps in the microstructure according to the atomic force microscopy and SEM images after the bending test, as shown in figure 7 [95]. In this model, under bending conditions, the uniaxial strain was assumed to induce disconnected points at the nanogaps of the $\beta\text{-Ga}_2\text{O}_3$ layer, which could severely hinder the current flow and result in high resistance. Interestingly, the authors found that the bending-induced microcracks and nanogaps can be healed through either thermal annealing or water-vapor treatment to recover the electrical performance to a great extent (figures 7(e)–(g)). The microcracks or nanogaps present in the $\beta\text{-Ga}_2\text{O}_3$ layers may reattach by van der Waals (vdW) interactions at high temperatures or chemical binding under a water-vapor atmosphere.

In another study, Zhang *et al* fabricated a similar $\beta\text{-Ga}_2\text{O}_3$ flexible device, as shown in figure 8(a) [92]. The only difference is that the target substrate was muscovite instead of a polymer. They found that the current increased as the bias voltage increased from 0 to 1 V because of an increased probability of electron transfer from $\beta\text{-Ga}_2\text{O}_3$ to Ni contacts owing to the reduced conduction band minimum of $\beta\text{-Ga}_2\text{O}_3$ under the bending condition; however, such

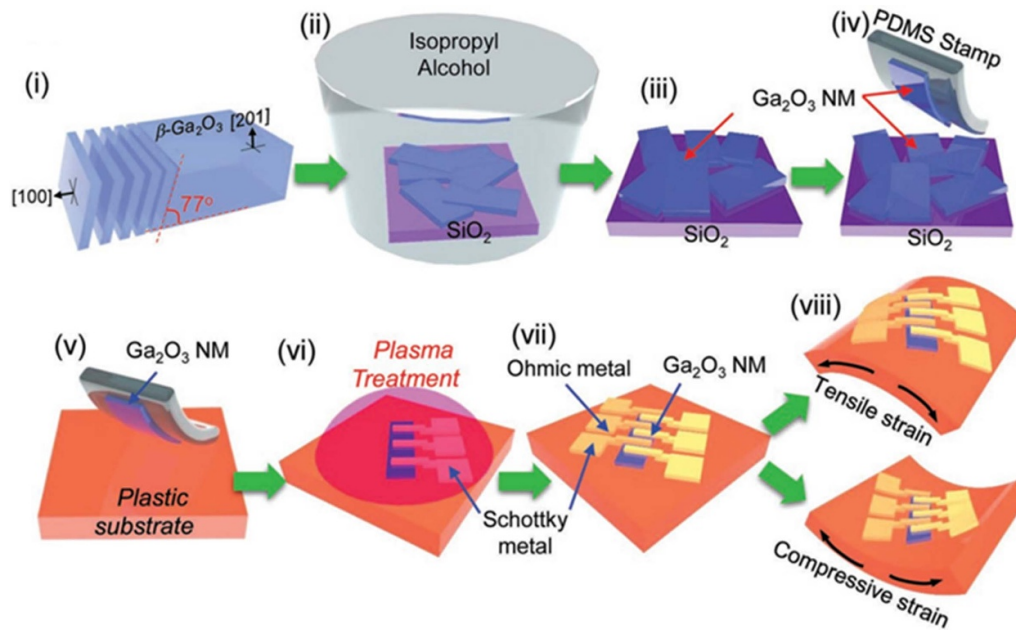


Figure 5. Fabrication of β -Ga₂O₃ Schottky barrier diodes: (i) cleaving process from bulk β -Ga₂O₃, (ii), (iii) additional sonification process to further thin down β -Ga₂O₃, (iv), (v) micro-transfer printing to relocate β -Ga₂O₃ nanomembranes onto a plastic substrate, (vi), (vii) metallization for ohmic and Schottky contacts, and (viii) illustration of the bending test [93]. Copyright 2019 WILEY-VCH.

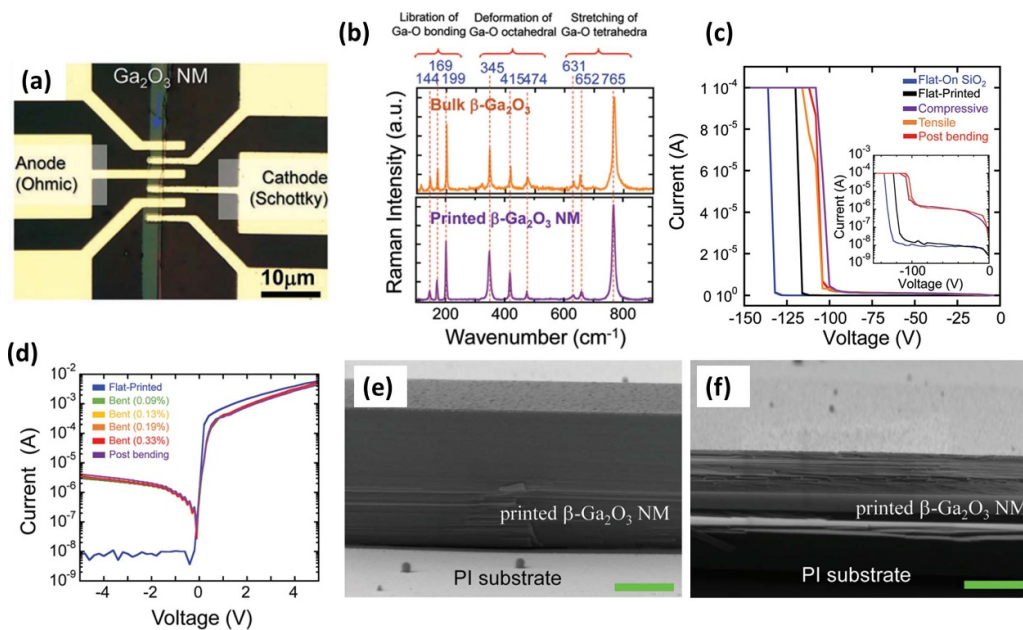


Figure 6. (a) Microscopic image of the finished β -Ga₂O₃ nanomembrane (NM) Schottky barrier diodes (SBDs). (b) Raman spectra of bulk β -Ga₂O₃ and printed β -Ga₂O₃ NMs showing no residual strain. (c) Breakdown voltage of flexible β -Ga₂O₃ SBDs under flat and bending conditions. The inset shows the I - V characteristics in logarithmic scale. (d) I - V characteristics of flexible β -Ga₂O₃ NM SBDs on a plastic substrate under compressive strains; angled scanning electron microscopy images of β -Ga₂O₃ NMs on a plastic substrate (e) before and (f) after the bending (>10 times). The scale bar is 200 nm [93]. Copyright 2019 WILEY-VCH.

influence was saturated when the bias voltage was >1 V, as shown in figure 8(b). The increased and unchanged current in low and high bias ranges, respectively, resulted in a degraded subthreshold swing (SS) under bending conditions (figure 8(c)). Their finding is valuable because the SS value is a key parameter for evaluating the on-off performance of transistors.

Other than SBDs, the transferred β -Ga₂O₃ can also be used to fabricate flexible PDs. The bending effect on the photoelectrical performance of flexible β -Ga₂O₃ PDs was systematically investigated by Lai *et al* as shown in figure 9 [96]. They showed a wavelength shift from 252 nm to 260 nm in the photoresponse spectrum, together with enhanced higher photoresponsivity when the PD was bent (figures 9(d)-(f)).

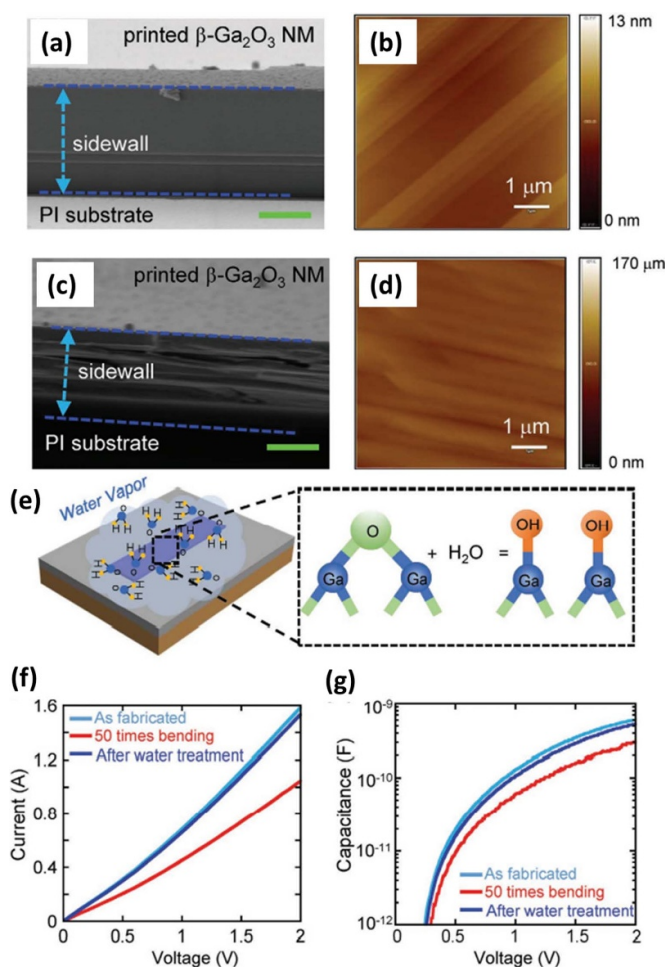


Figure 7. Angled scanning electron microscopy (SEM) and atomic force microscopy images of β -Ga₂O₃ nanomembrane (NM) on a polyimide substrate (a), (b) before and (c), (d) after the bending that show cracks on the sidewall of β -Ga₂O₃ NM. The scale bars in SEM images are 200 nm. (e) Illustration of water-vapor treatment on β -Ga₂O₃. The inset shows the modification of β -Ga₂O₃ to OH bonds. (d) I - V and (e) C - V characteristics measured before and after water-vapor treatment [95]. Copyright 2021 WILEY-VCH.

According to a comprehensive structural analysis and density functional theory calculations, the shift was caused by the changes in the refractive index and the extinction coefficient formation of β -Ga₂O₃, whereas the enhanced photoresponsivity was caused by secondary light absorption at the nanogaps upon bending (figures 9(g) and (h)).

Further, Li *et al* explored the application of Ga₂O₃ in flexible PDs [94]. In their study, using transferred β -Ga₂O₃ as the channel layer and transferred BN as the dielectric layer, they fabricated a flexible phototransistor (figure 10(a)). Here, the phototransistor can be understood as a combination of the PD and TFT; that is, the device can display excellent on/off behavior under illumination at a specific wavelength range. The phototransistor showed high responsivity, large detectivity (D^*), and ultrafast response, superseding those of conventional Ga₂O₃ PDs (figures 10(b) and (c)). More importantly, they fabricated an array of Ga₂O₃ phototransistors, realizing a UV detector composed of 15×15 pixels. By

combining the detector array with an artificial neural network, the system can be used for image recognition in robots (figure 10(d)).

Manual mechanical cleavage is an inevitable step for typical transfer routes. However, the thickness of the cleaved layer can be random because it depends on the habits of the operator [93, 95]. Such disadvantages make the typical transfer route incompatible with scaling. To solve this problem, Wang *et al* used water-soluble Sr₃Al₂O₆ as the buffer layer to grow free-standing Ga₂O₃ flexible membranes [91]. Using this strategy, Sr₃Al₂O₆ was first deposited on a conventional rigid substrate; then, Ga₂O₃ thin films were deposited on top of Sr₃Al₂O₆. Because the stacked structure was grown using an additive deposition route, the thickness of the Ga₂O₃ thin film was controlled by tuning the deposition time, temperature, and other parameters. After deposition, Sr₃Al₂O₆ was easily removed by rinsing the stacked structure in water because it is water-soluble. Upon the removal of the Sr₃Al₂O₆ buffer layer, Ga₂O₃ was dispatched from the rigid substrate, yielding a free-standing flexible Ga₂O₃ membrane. The whole fabrication procedure is illustrated in figure 11(a). However, in Wang *et al*'s research, the Sr₃Al₂O₆ and Ga₂O₃ thin films were deposited via sputtering at room temperature; thus, they remained either polycrystalline or amorphous. Such poor crystal quality is against the original purpose of the transfer method, which is to ensure single-crystalline Ga₂O₃. Although single-crystalline Ga₂O₃ could not be obtained, the Sr₃Al₂O₆ buffer layer method remains promising. Sr₃Al₂O₆ has a cubic structure, as shown in figure 11(b) [104]. The epitaxial relationship between β -Ga₂O₃ (-201)- and cubic (001)-structured thin films has been demonstrated [105–108]. Moreover, Sr₃Al₂O₆ has a high thermal stability of up to 800 °C (figure 11(c)) [109]. Therefore, a single-crystalline β -Ga₂O₃ (-201) thin film can be obtained on Sr₃Al₂O₆ (001) at high temperatures using PLD, MOCVD, and MBE.

5. Amorphous Ga₂O_x grown *in situ*

To overcome the complexity and irreproducibility of the transfer technique, the straightforward route is used to deposit Ga₂O₃ thin films on flexible substrates *in situ*. However, the thermal stability of conventional polymer substrates cannot meet the requirements for the high-temperature growth of β -Ga₂O₃. Hence, amorphous Ga₂O_x thin films can be deposited at room temperature [110–120]. Compared with β -Ga₂O₃, amorphous Ga₂O_x has relatively low thermal stability, and its stoichiometry is variable and highly dependent on deposition parameters [110–112].

Liang *et al* [110] Cui *et al* [111] and Wang *et al* [112] varied the Ga/O ratio to improve the performance of amorphous Ga₂O_x. They grew amorphous Ga₂O_x thin films directly on PEN substrates at room temperature by controlling the oxygen flux. The samples were then fabricated into flexible PDs by depositing ITO contacts on the surface, as shown in figure 12(a) [111]. The photocurrent and the dark current decreased with the oxygen partial pressure. For instance, by increasing the oxygen partial pressure from 0 sccm (sample

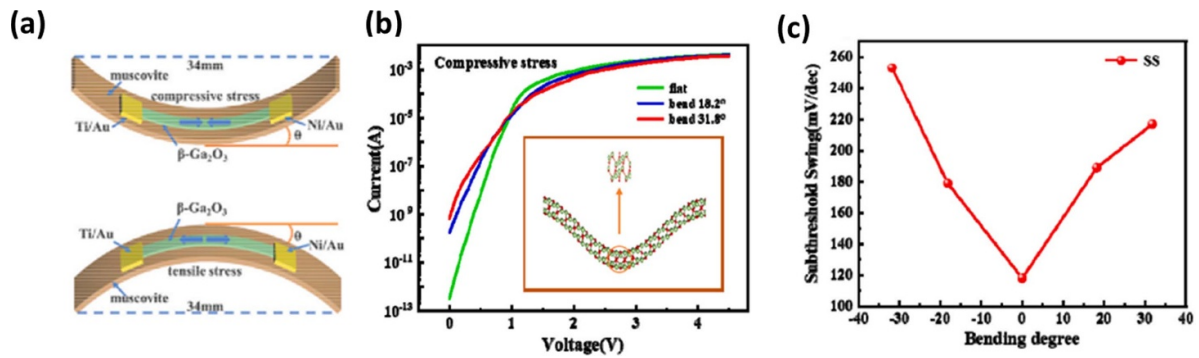


Figure 8. (a) Flexible β -Ga₂O₃ Schottky barrier diode (SBD) based on muscovite under upward and downward bending. (b) I - V curves of muscovite with transverse β -Ga₂O₃ SBD in upward bending of 18.2, 31.8, and flat state. Inset: upward bending structure diagram of β -Ga₂O₃ and some enlarged molecular structures. (c) Subthreshold swing of different bending degrees [92]. Copyright 2021 Elsevier.

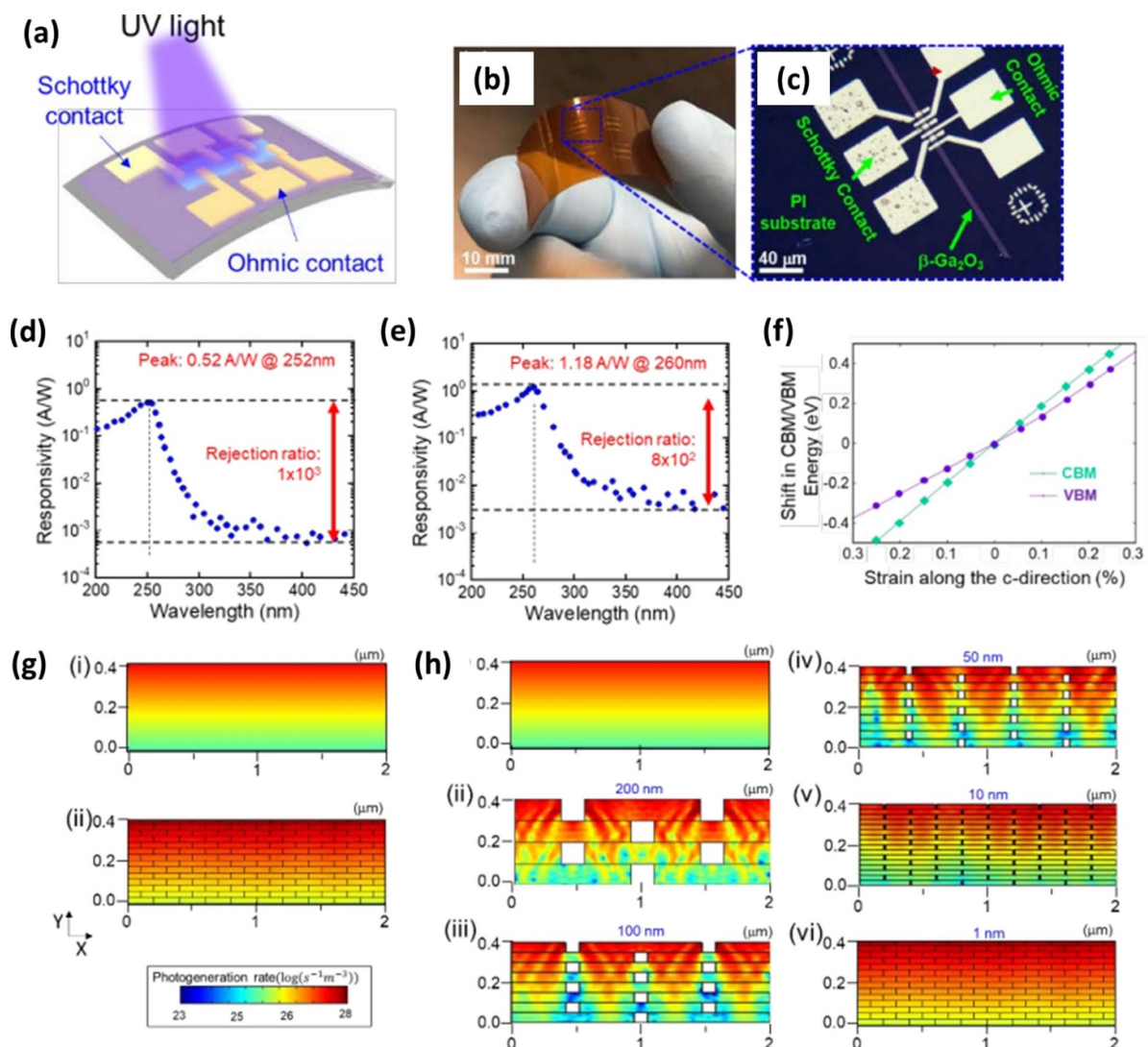


Figure 9. (a) β -Ga₂O₃ nanomembrane (NM) photodetector (PD) under the bending test. (b) Photograph of the fabricated β -Ga₂O₃ NM PD under the bending condition. (c) Microscopic image of the finished β -Ga₂O₃ NM PDs. (d) Photoresponse spectrum of the β -Ga₂O₃ NM PD under a flat condition at a voltage bias of -5 V. (e) Photoresponse spectrum of the β -Ga₂O₃ NM PD under the bending condition at a bias voltage of -5 V. (f) Shift in conduction band minimum/valence band maximum energy as a function of local uniaxial strain. (g), (h) Simulated photogeneration of β -Ga₂O₃ NMs on a polyimide substrate under different bending conditions. (g) (i) Before and (ii) after the formation of nanocracks in β -Ga₂O₃ NM. (h) Simulated photogeneration rates with gap distances of (i) 0 nm, (ii) 200 nm, (iii) 100 nm, (iv) 50 nm, (v) 10 nm, and (vi) 1 nm in β -Ga₂O₃ NMs [96]. Copyright 2020 RSC.

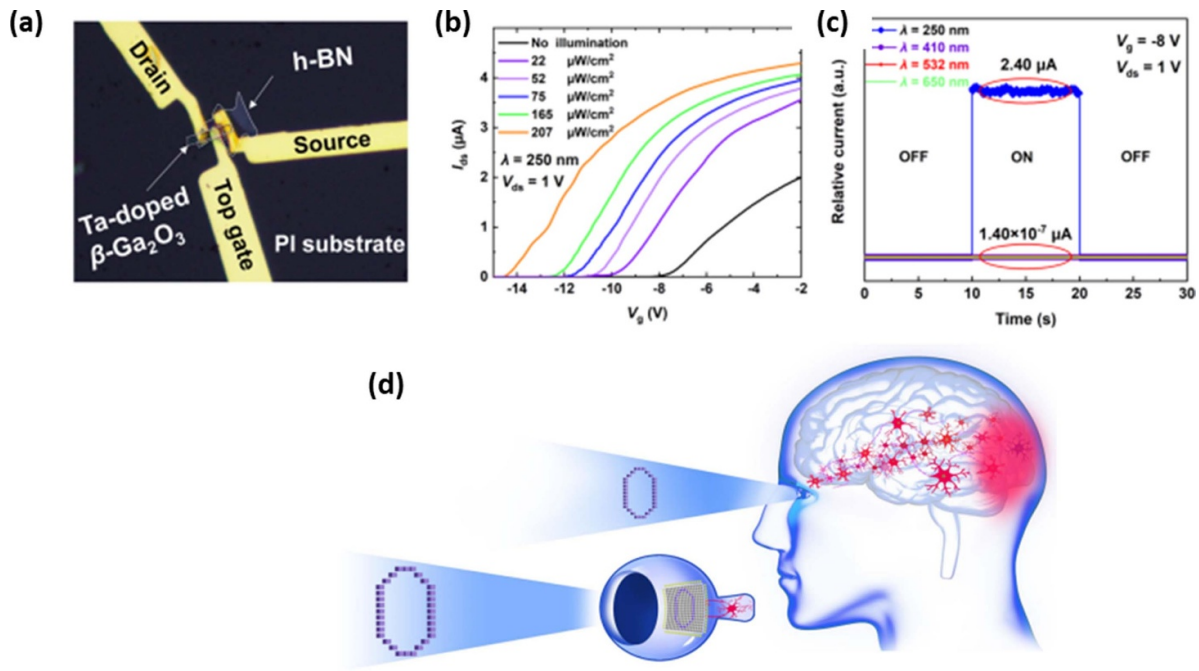


Figure 10. (a) Optical microscopy image of the fabricated β -Ga₂O₃ transistor. (b) Transfer characteristics of the device under dark and different illumination power intensities (P_{in}) at $V_{ds} = 1$ V. (c) Time-dependent photoresponse of the β -Ga₂O₃ device under different wavelengths at $V_{ds} = 1$ V and $V_g = -8$ V. (d) Schematic of the simulation of the human nerve visual system [94]. Copyright 2022 Nature Springer.

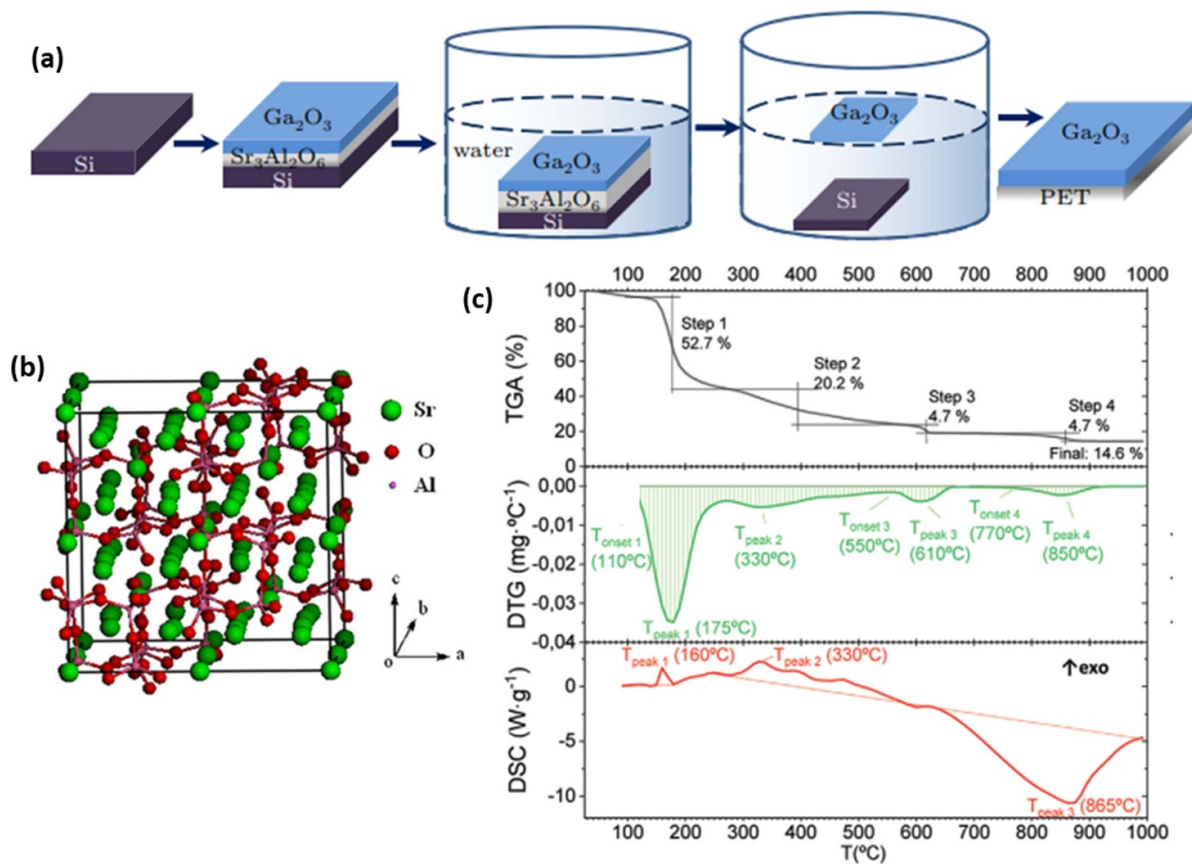


Figure 11. (a) Schematic of free-standing Ga₂O₃ thin film fabrication [91] Copyright 2019 IOP science. (b) Lattice structure of Sr₃Al₂O₆ [104] Copyright 2013 Elsevier. (c) Thermogravimetric analysis, its derivative thermogravimetry, and differential scanning calorimetry of the precursor solution of Sr₃Al₂O₆ [109]. Copyright 2021 WILEY-VCH.

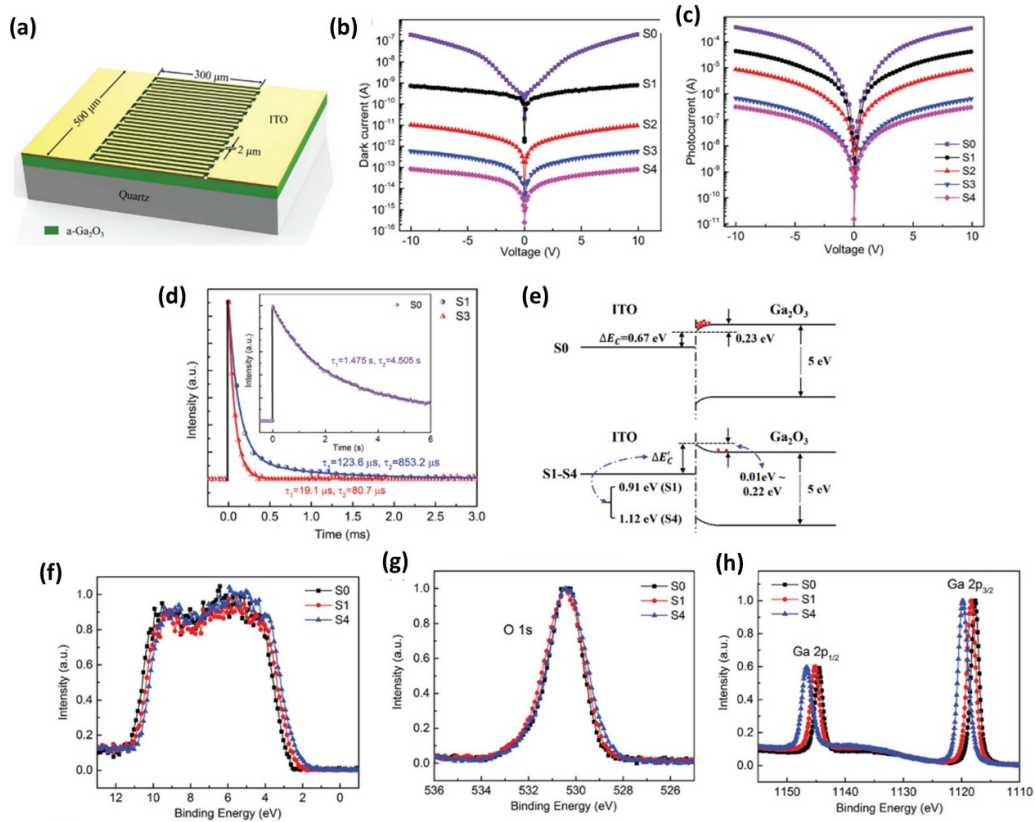


Figure 12. (a) Schematic of the Ga₂O₃-based metal-semiconductor-metal photodetector (PD). (b) I - V curves in dark and (c) under ultraviolet 254 nm light illumination. (d) Temporal response tests of PDs with krypton fluoride pulse laser illumination at 10 V bias. (e) Schematic energy band diagrams of the ITO/Ga₂O₃ interface. (f) Normalized x-ray photoelectron spectroscopy (XPS) valence band spectra of a-Ga₂O₃ films. (g) Normalized O 1s and Ga 2p. (h) XPS spectra of a-Ga₂O₃ films [111]. Copyright 2017 WILEY-VCH.

S0) to 0.15 sccm (sample S4), the dark current and the photocurrent of the flexible PDs decreased from 10^{-6} A to 10^{-13} A and from 10^{-3} to 10^{-10} A, respectively, and the response time was shortened from seconds to tens of microseconds (figures 12(b)–(d)). The ultraslow response observed on S0 is known as the persistent photocurrent (PPC) and is regarded as the main drawback of amorphous Ga₂O_x PDs [33]. For a detailed understanding of the effect of oxygen on the photoelectrical performances of flexible PDs, x-ray photoelectron spectroscopy (XPS) was performed on the samples deposited using different oxygen fluxes, as shown in figures 12(f)–(h). First, the normalized XPS valence band spectra indicated that the valence band gradually shifted toward the lower binding energy with the increased oxygen flux. Using the linear extrapolation method, the valence band maximum values for the sample deposited without and with the highest oxygen flux were obtained as 2.73 eV and 2.28 eV, respectively. Hence, an upward bending value of 0.45 eV was deduced for the valence band maximum and conduction band minimum values. Using the bandgap (E_g) and electron affinity (χ) for Ga₂O_x and the work function of ITO as 5 eV, 4 eV, and 4.9 eV, respectively, the schematic energy band diagrams for S0 and S4 are shown in figure 12(e). The surface energy band for S0 bent downward by 0.23 eV, resulting in a Schottky barrier (ΔE_C) of 0.67 eV, whereas for S4, the surface energy band bent upward by 0.22 eV, resulting in a Schottky barrier ($\Delta E'_C$) of

1.12 eV. High SB is responsible for the decreased photocurrent and dark current in S4 obtained by blocking the movement of photoinduced electrons from Ga₂O₃ to ITO. Furthermore, the O 1s and Ga 2p emissions of the samples are shown in figures 4(c) and (d). By integrating the enveloped area of the O 1s and Ga 2p peaks, the ratio SO_{1s}/SGa_{2p} was calculated as 0.61 and 0.65 for S0 and S4, respectively, suggesting higher oxygen content and lower oxygen vacancies in S4. In oxide PDs, oxygen vacancies serve as deep-level trapping centers; hence, the decreased oxygen vacancies enhance the response speed, thereby eliminating the PPC effect.

A similar structure for flexible x-ray detectors was also demonstrated [110]. Upon x-ray illumination, high-energy electrons are generated throughout the Ga₂O_x thin film owing to the high penetrability of x-rays. The schematic energy band diagrams illustrating the conductive electrons released from the valence band, valence bond theory states, and ionization of Vo under UV and x-ray radiation are shown in figure 13. In the vicinity of the thin film surface, such high-energy electrons may escape from Ga₂O_x, inducing a surface photochemical reaction and an air ionization effect. Such photochemical reactions can change the Ga/O stoichiometry of the materials, thus affecting the long-term stability of the devices. For high-energy electrons generated far below the surface, owing to the considerably higher energy of x-rays compared with UV light, their excessive energy can be effectively transferred to

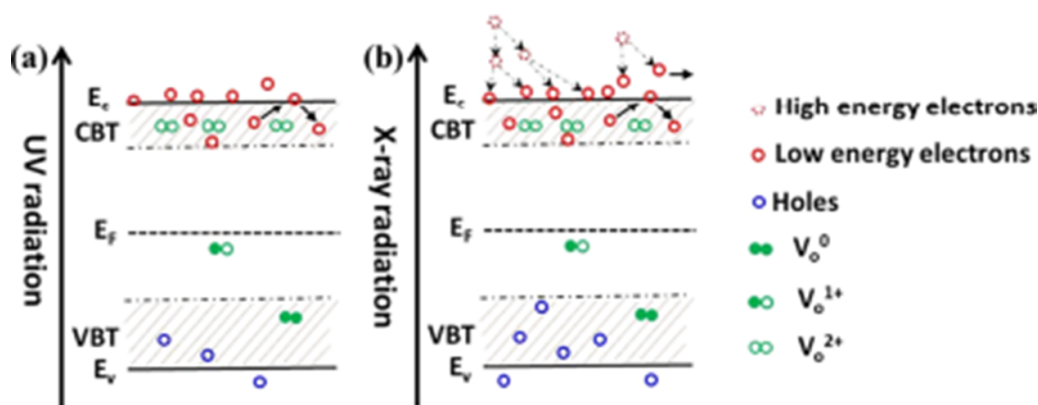


Figure 13. Schematic energy band diagrams illustrating conductive electrons released from the valence band, valence bond theory states, and ionization of V_o under (a) ultraviolet and (b) x-ray radiation, respectively [110]. Copyright 2019 ACS.

nearby atoms. Such a process affords additional e–h pairs and enhances the photocurrent induced by x-ray illumination. In this research, the effect of oxygen flux on photoelectrical performance was investigated. Similarly, for x-ray detectors, the photocurrent, dark current, and response time decreased with oxygen flux, in line with the aforementioned oxygen vacancy mechanism. In addition, in another study by Li *et al* oxygen vacancies were adjusted by moderately elevating the deposition temperatures up to 200 °C [116]. However, the temperature must be below the decomposition temperatures of polymer substrates.

Another route to modify the performance of amorphous flexible Ga_2O_x PDs is to construct a heterostructure by depositing other semiconductor layers on top of or beneath the Ga_2O_x layers [113–115, 119]. For instance, heterostructures, including Ga_2O_x/MoS , Ga_2O_x/ZnO , Cu_2O/Ga_2O_x , and $Al/Al_2O_3/Ga_2O_x$, have been investigated, where the additional layers were deposited at low temperatures owing to the low thermal stability of polymer substrates; thus, they remained amorphous or polycrystalline. In detail, the Ga_2O_x/MoS improved the photocurrent in the DUV region by modifying the carrier behaviors at the Ga_2O_x/MoS interfaces; the Ga_2O_x/ZnO showed enhanced photocurrent and response time under tensile strain by taking advantage of the piezoelectric effect of ZnO ; because Cu_2O is a p-type semiconductor and Ga_2O_x is an intrinsic n-type semiconductor, Cu_2O/Ga_2O_x realized self-powered DUV PDs upon the formation of a p–n junction; the Al/Al_2O_3 multilayer maximized the absorption efficiency and thus the responsivity of Ga_2O_x when the Al/Al_2O_3 destructive interference overlapped with the Ga_2O_x absorption edge.

Most recently, Wang *et al* [112] integrated these Ga_2O_x PDs with a full-wave bridge rectifier and a receiving electrode to construct a flexible self-powered DUV detection system, as shown in figure 14. The power source of the system was the human body–absorbed ambient electromagnetic radiation energy. The radiation resulted in an inductive current, which was received by the electrode, rectified by the full-wave bridge rectifier, and eventually supplied to the connected PDs. The

self-powered PD had a good photoelectrical performance with responsivity and detectivity of 0.1 A W^{-1} and 2.24×10^{11} Jones, respectively. However, the light-to-dark ratio was only 8.31. In contrast, the light-to-dark ratio obtained from the conventional bias-powered Ga_2O_x PD is usually $>10^5$ [3, 57].

To utilize flexible Ga_2O_x PDs in actual applications, such as solar-blind imaging, obtaining the spatial distribution of the light source intensity, and real-time light trajectory detection, the PDs must be fabricated into arrays comprised of multiple PD diodes, which require flexible Ga_2O_x thin films with low roughness, homogeneous material quality, and low performance variation between individual diodes on a large scale. Compared with the complicated transfer technique, the *in situ* growth of amorphous Ga_2O_x has a great advantage in that it can ensure the large-scale deposition of homogeneous Ga_2O_x thin films on which conventional photolithography patterning can be performed to create photodetection arrays. Following this strategy, Chen *et al* fabricated a large-scale Ga_2O_x PD array with an area of $0.9 \text{ mm} \times 0.9 \text{ mm}$ containing 7×7 rectangular cells on PEN substrates, as shown in figure 15 [119]. For the actual imaging applications, first, they examined the performance uniformity of the PD cells, which was statistically described using the coefficient of variation (CV), which is defined as the percentage of the standard deviation and the mean value of a set of data. As shown in figure 15(a), the dark currents of all PD cells were in the range of $15 \pm 2.5 \text{ pA}$, yielding a CV of 6.9%, whereas the photocurrents of all PD cells were in the range of $13 \pm 1.2 \text{ pA}$, yielding a CV of 6.9%, which indicated high uniformity of the PD array. A photomask with an E-shaped hollow pattern was covered on the PD array to test the actual imaging performance. Upon 254 nm light illumination, the PD array showed a clear E shape, suggesting good imaging ability, as shown in figure 15(b). To test the sensitivity of the array to light intensity, the photomask was removed, and only a narrow single beam was subjected to the center of the array. The response photocurrent distribution of the PD array is shown in figures 15(c) and (d), which provided a clear 2D mapping of the illuminated light intensity. To test the real-time light-tracing capability of the PD array,

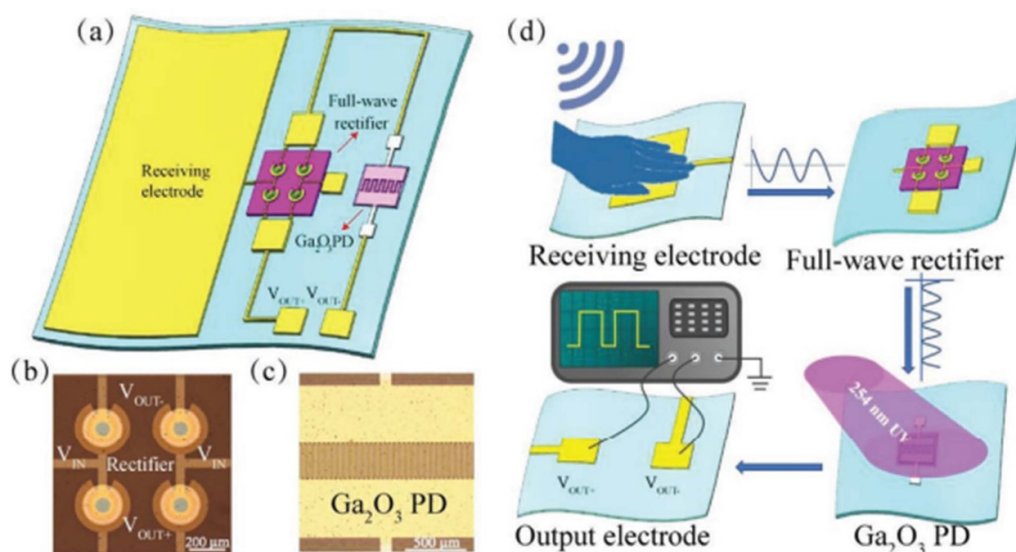


Figure 14. (a) Schematic of the integrated system fabricated on a $25 \times 25 \text{ mm}^2$ polyethylene naphthalate substrate. (b) Microscopy image of the full-wave bridge rectifier. (c) Microscopy image of the $\alpha\text{-Ga}_2\text{O}_3$ ultraviolet photodetector. (d) Schematic of the workflow of the integrated self-powered ultraviolet detection system [112]. Copyright 2021 WILEY-VCH.

a single light beam was moved from cell 1 to cell 7. Correspondingly, the current of the single PD cell increased upon illumination and then decreased when the source of illumination moved away. As the beam moved, the currents of the PD cells increased and then decreased from cell 1 to cell 7 in the same order.

To further explore the application of flexible Ga_2O_x PDs, Chen *et al* fabricated a 3D array by employing the origami/kirigami technique, as shown in figure 16 [118]. Compared with the 2D array, the 3D counterparts offered unique advantages, such as an extremely wide detection space angle and excellent spatial recognition. The uniformity test performed on the 3D array provided a CV of only 3.5%, which is lower than that of its 2D counterpart. Further, in the actual detection examinations, the 3D array showed unique capabilities, such as multiple light signal detection, arc signal movement, and altitude change movement, as shown in figure 16.

In addition to PDs, amorphous Ga_2O_x flexible thin films can be used in flexible memory and TFTs [120]. The fabrication of flexible TFT devices by Qian *et al* [57] is particularly interesting because TFTs have a more sophisticated device structure than PDs and chemical solution deposition (CSD) instead of RF deposition was employed for the growth of Ga_2O_x . Compared with the RF route, the CSD route offers cost-effectiveness, high production speed, compatibility with the reel-to-reel system, and scalability [121–123]. The actual large-scale reel-to-reel system for producing yttrium barium copper oxide (YBCO) superconductor tapes via CSD is shown in figure 17 [124, 125]. Moreover, CSD allows the adjustment of chemical composition. For instance, indium or aluminum can be easily doped in the Ga_2O_x thin film to tune the bandgap or device performance by adding $\text{In}(\text{NO}_3)_3$ or $\text{Al}(\text{NO}_3)_3$ to the $\text{Ga}(\text{NO}_3)_3$ precursor [47]. In general, the fabricated TFT device showed excellent on/off transition behaviors, including

a low threshold voltage of 0.61 V, low SS of 0.5 V dec^{-1} , and high mobility (μ_{sat}) of $2.74 \text{ cm}^2 \text{ V}^{-1} \text{ s}^{-1}$.

6. Epitaxial films grown *in situ*

As described above, the transfer technique can ensure high crystal quality at the price of scaling and reproducibility. In the *in situ* room-temperature deposition route, Ga_2O_x thin films are directly grown on flexible polymer substrates. However, because of the low deposition temperature limited by the low thermal stability of polymer substrates, the grown films remain amorphous, with oxygen vacancies highly dependent on the oxygen flux during deposition, resulting in unpredictable photoelectrical performance. To realize the *in situ* growth of single-crystalline oxide thin films, high thermal stability up to the temperature range for the crystallization of oxide ceramic materials and ideal lattice match with the oxides are required [126–130].

As shown in figure 4, Hastelloy flexible substrates can meet the thermal stability requirements for the crystallization of $\beta\text{-Ga}_2\text{O}_3$ because its melting deposition is up to 1300°C . However, Hastelloy substrates are polycrystalline and thus cannot serve as epitaxial templates for $\beta\text{-Ga}_2\text{O}_3$. Functionalization with an additional single-oriented ceramic buffer layer is a feasible route for endowing them with an ideal lattice constant for the epitaxial growth of $\beta\text{-Ga}_2\text{O}_3$ [131–136]. The most commonly adopted growing facet of $\beta\text{-Ga}_2\text{O}_3$ is (-201) , the atomic distribution of which has a six-fold symmetry. Therefore, the epitaxial deposition of high-quality single-oriented $\beta\text{-Ga}_2\text{O}_3$ (-201) thin films has been demonstrated on sapphire (0001), yttrium-stabilized zirconate (111), and 3 C-SiC (001), all of which have the symmetry of an integer multiple of three [1, 3, 33, 105]. However, the growth of such

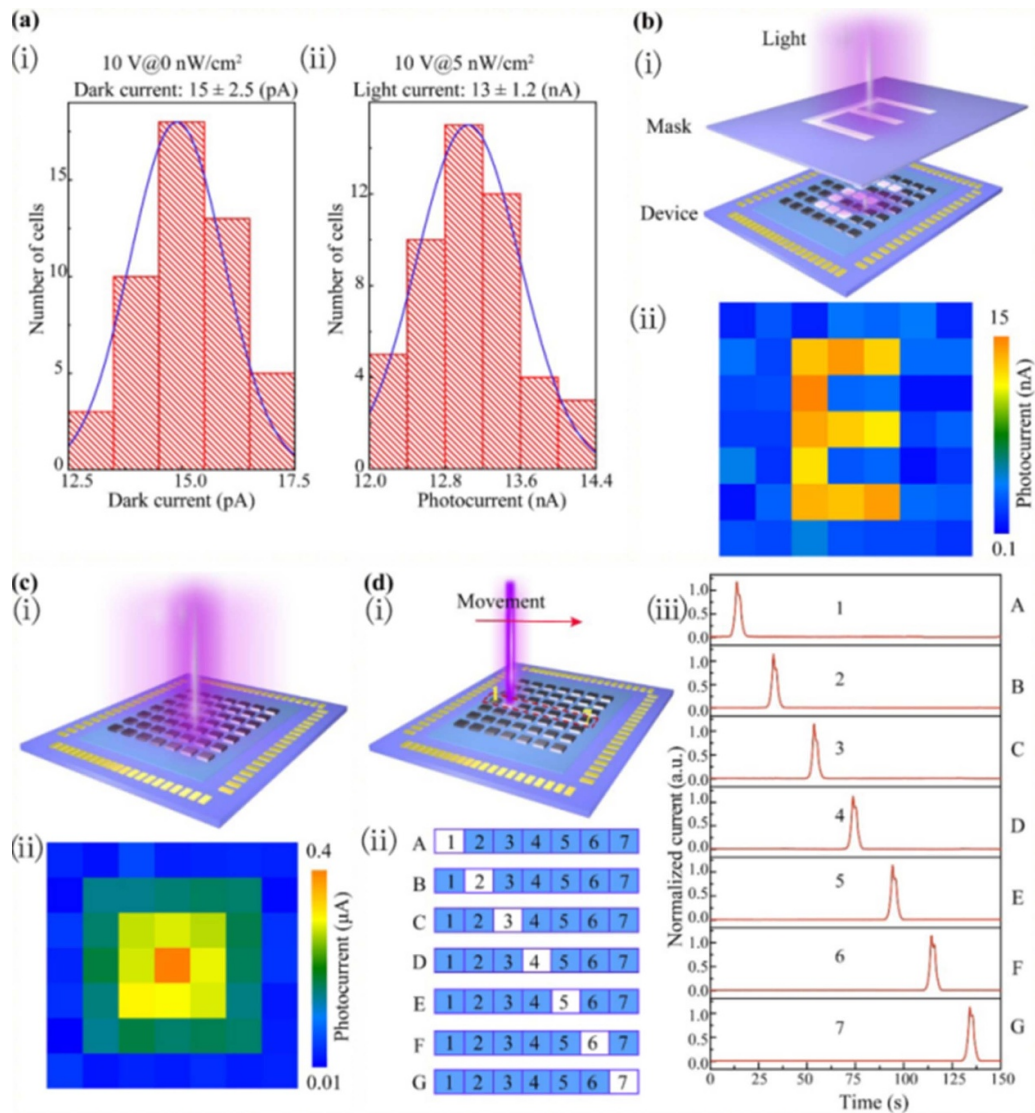


Figure 15. Use of a photodetector array for light imaging, spatial distribution of light source intensity, and real-time light trajectory detection. (a) (i) Statistical dark current and a) (ii) photocurrent under 254 nm illumination with an intensity of 5 nW cm^{-2} of the photodetector cells at 10 V bias. (b) (i) Schematic of imaging data acquisition and (b) (ii) image acquired from the photodetector array with an optical pattern of 'E'. (c) (i) Schematic of the spatial distribution detection of light source intensity and c) (ii) mapping results obtained from the photodetector array. (d) Demonstration of the real-time light trajectory: (d) (i) schematic of the light spot movement, (d) (ii) corresponding trajectory (from cell 1 to cell 7), and (d) (iii) variation in terminal output current when the light spot goes through the corresponding cells [119]. Copyright 2022 Springer.

three-fold-symmetry ceramic layers has not been realized on Hastelloy substrates. Recently, Tang *et al* demonstrated the epitaxial growth of $\beta\text{-Ga}_2\text{O}_3$ (-201) on CeO_2 (001), which has four-fold symmetry [105]. They found that the obtained $\beta\text{-Ga}_2\text{O}_3$ (-201) thin films comprised two sets of hexagonal-like frameworks with a mutual rotation angle of 90° . This is attributable to the small lattice mismatch between the $\beta\text{-Ga}_2\text{O}_3$ (201) plane and the CeO_2 (001) plane in two directions: CeO_2 [100]// $\beta\text{-Ga}_2\text{O}_3$ [010] and CeO_2 [010]// $\beta\text{-Ga}_2\text{O}_3$ [010]. The epitaxial relation between $\beta\text{-Ga}_2\text{O}_3$ (-201) and CeO_2 (001) is depicted in figure 18(a).

Based on these findings, Tang *et al* [105] further explored the epitaxial deposition of $\beta\text{-Ga}_2\text{O}_3$ (201) thin films on CeO_2

(001)-functionalized Hastelloy substrates. The functionalization procedure was developed and employed in flexible coated-conductor production [87, 88]. In general, the CeO_2 (001)-functionalized Hastelloy tape has a multilayer stacked structure, as shown in figure 18(b). To construct such a structure, first, the tape was coated with amorphous Al_2O_3 (80 nm) and Y_2O_3 (20 nm) layers successively using reactive RF sputtering. Here, the Al_2O_3 layer serves as a barrier to minimize the diffusion of metallic elements during subsequent high-temperature treatments, whereas the Y_2O_3 layer serves as a seed layer for the following deposition of crystallized epitaxial layers. Next, a highly crystallized MgO (001) layer (5 nm) was realized using the IBAD technique. Thereafter,

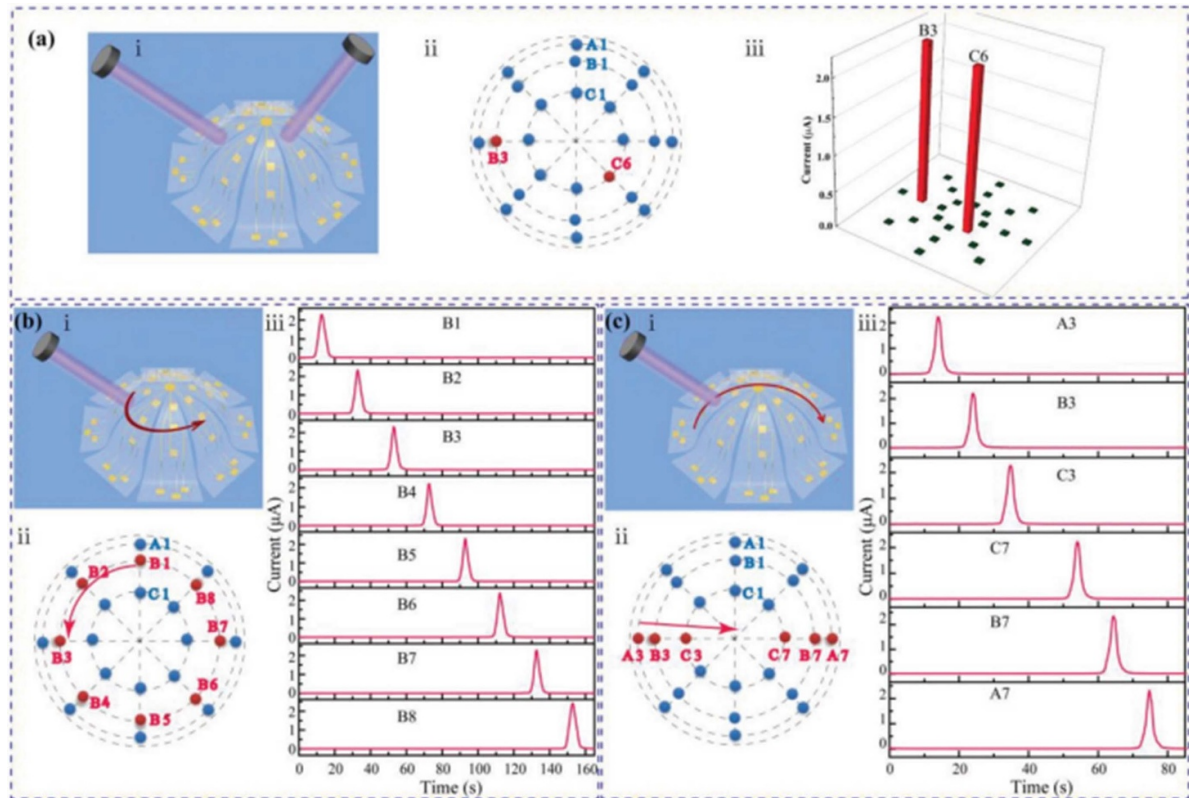


Figure 16. (a) (i) Schematic of a 3D photodetector with two beams incident simultaneously. (a) (ii) Plane view of the irradiation positions of the two beams. (a) (iii) Photocurrent distribution on the hemispherical surface of the 3D photodetector. (b) (i), (c) (i) Schematic of the measurement of the real-time light trajectory. (b) (ii), (c) (ii) Plane views obtained during the test procedures. (b) (iii), (c) (iii) Currents of the corresponding photodetector cells during the movement of the light beam [118]. Copyright 2019 WILEY-VCH.

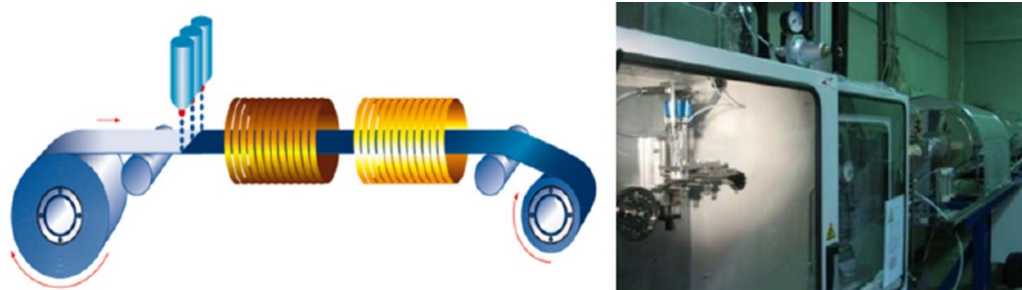


Figure 17. Continuous reel-to-reel electromagnetic ink-jet printing system and subsequent online thermal treatment. Schematic (left) and photograph (right) of the pilot production facilities in Deutsche Nanoschicht [124]. Copyright 2012 IOP Publishing.

LaMnO₃ (20 nm) and CeO₂ (200 nm) layers were successively deposited via RF sputtering. The LaMnO₃ layer created a lattice gradient from MgO to CeO₂ and enhanced the bi-axial texture of CeO₂ (001). Finally, β -Ga₂O₃ (-201) was grown using PLD at 680 °C, which is much higher than that used in RF deposition for amorphous Ga₂O_x thin films. The two-theta, rocking curve, and phi-scan XRD results are shown in figures 18(c)–(e). The obtained tapes were also fabricated into flexible PDs. The PDs showed a responsivity of 4×10^4 mA ⁻¹ W with an on/off ratio reaching 1000 under 254 nm incident light and 5 V bias voltage. The obtained photoelectrical performance is comparable with

those of β -Ga₂O₃-based PDs fabricated using conventional rigid single-crystalline substrates. Time-resolved photocurrent measurements were performed under different bending radii, and the results are shown in figure 18(f).

We can conclude that flexible substrates that are promising for the epitaxial growth of Ga₂O₃ films must possess i) high material quality, ii) smooth surface, and iii) high-temperature stability. Muscovite mica (KAl₂(Si₃Al)O₁₀(OH)₂), which possesses high-temperature tolerance, great flexibility, high transparency, high crystallinity, and satisfactory thermal stability, can be used for the *in situ* epitaxial growth of Ga₂O₃. Its aluminosilicate and layered structure allows for artificial

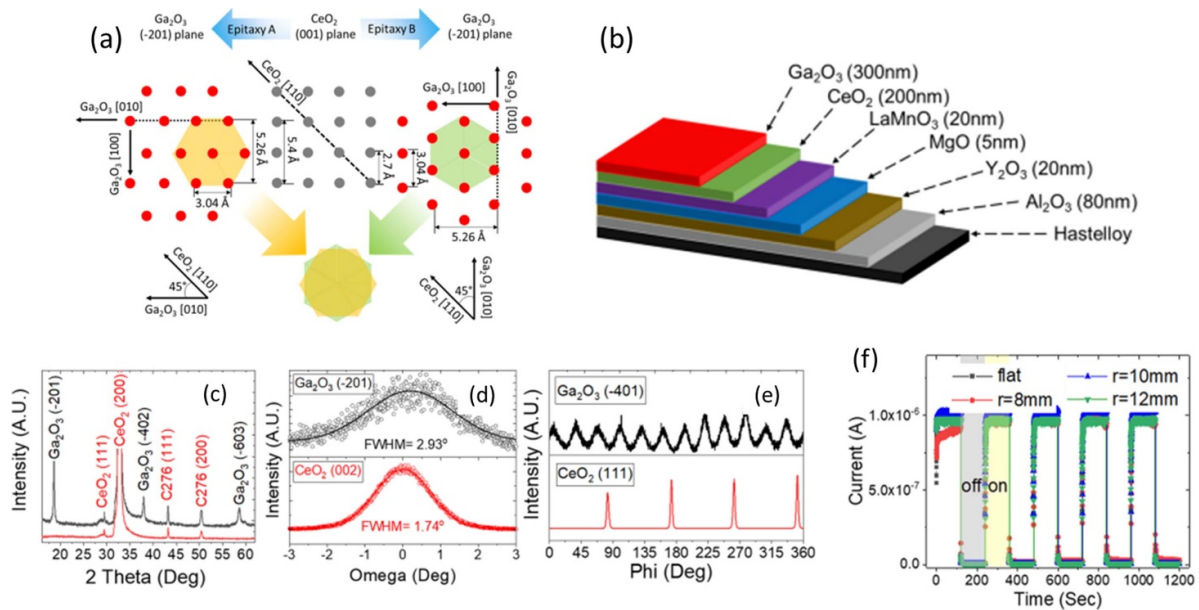


Figure 18. (a) In-plane epitaxial relationship between CeO_2 (001) and Ga_2O_3 (-201). The gray and red dots represent the oxygen atom distribution in the CeO_2 (001) and $\beta\text{-Ga}_2\text{O}_3$ (-201) planes, respectively. The orange and green areas represent the smallest six-fold-symmetric hexagon units in the $\beta\text{-Ga}_2\text{O}_3$ (-201) plane for epitaxy A and B, respectively. (b) Cross-sectional schematic of the layer configuration of the $\beta\text{-Ga}_2\text{O}_3$ -coated flexible tape. (c) Out-of-plane 2θ x-ray diffraction patterns of the $\beta\text{-Ga}_2\text{O}_3$ -coated tape (black) and CeO_2 -buffered Hastelloy tape (red). (d) Rocking curves of $\beta\text{-Ga}_2\text{O}_3$ (-201) (black) and CeO_2 (002) (red) of the $\beta\text{-Ga}_2\text{O}_3$ -coated tape, where the lines represent the Gaussian fitting of the measured data points. (e) ϕ -scan of the $\beta\text{-Ga}_2\text{O}_3$ (-401) plane (black) and the CeO_2 (111) plane (red) of the $\beta\text{-Ga}_2\text{O}_3$ -coated tape. (f) Time-dependent photoresponse curves measured under 254 nm illumination by periodically turning on/off at 120 s intervals [35]. Copyright 2022 ACS.

exfoliation on an exceptionally large wafer scale, resulting in an atom-level flat surface without dangling bonds. Therefore, under high temperatures, the physisorption of atoms leads to deposition and crystallization on mica, resulting in a single-crystalline epitaxial layer, i.e. a vdW epitaxy [126].

The synthesis of Ga_2O_3 on mica was conducted at 600 °C using PLD by Tak *et al* [137]. The polycrystalline Ga_2O_3 film provided a 9.7 A W^{-1} photoresponsivity under 270-nm illumination [137]. Sui *et al* also demonstrated a flexible transparent Ga_2O_3 solar-blind UV PD using thermal annealing on mica and obtained robust flexibility (10 000 cycles in a fatigue test) [138]. Nevertheless, the device performances from both these works were insufficient due to the noncrystalline or polycrystalline structure of Ga_2O_3 . Tak *et al* demonstrated single-oriented β -phase Ga_2O_3 epitaxially grown on mica, but the performance of the fabricated PD was poor owing to the low material quality under the growth temperature of ~ 550 °C [139]. This is attributed to the ultrahigh synthesis temperature of the most thermodynamically stable β -phase Ga_2O_3 , which is usually beyond the mica substrate tolerance, i.e. 750 °C, for achieving high crystallinity and low defect density [62]. Accordingly, Lu *et al* [140] demonstrated a metastable κ -phase Ga_2O_3 (002) thin film on mica under 680 °C with high quality and high thermal stability. The epitaxy of κ -phase Ga_2O_3 was enabled by metal-oxide-catalyzed epitaxy, i.e. SnO_2 was incorporated in Ga_2O_3 as a metal-oxide source [141] (figure 19(a)). It provides a new perspective in that the κ -phase

Ga_2O_3 can be used in flexible Ga_2O_3 electronics in addition to the β -phase Ga_2O_3 . Moreover, the demonstrated flexible PD has a record high responsivity (703 A W^{-1}), on/off ratio ($>10^7$), detectivity (4.08×10^{14} Jones), and external quantum efficiency ($3.49 \times 10^5\%$), demonstrating the significant potential of the κ -phase Ga_2O_3 for ultrahigh-performance wearable oxide optoelectronics (figures 19(b) and (c)). Another superior property of the Ga_2O_3 /mica film is its highly robust flexibility. As shown in figures 19(b) and (d), the fabricated flexible PD possessed stable performance when considering bending radii of <1 cm and mechanical stability in case of 10 000 bending test cycles (figure 19(d)). This is attributable to the film's extraordinary flexibility and interlayer sliding ability to sufficiently release the strain in the epitaxial layer when the substrate-layer composite was bent.

In general, mica and Hastelloy substrates pave the way for the *in-situ* growth of crystalized Ga_2O_3 for flexible devices. Each of them has unique advantages. For mica substrate, because of its single-crystalline nature, high-quality Ga_2O_3 thin film with both in-plane and out-of-plane orientation can be readily obtained; different from mica, the Hastelloy substrate as a metallic material, has a much higher tensile strength, hence might be more promising in actual flexibility-required applications. However, due to its polycrystalline nature with no preferred orientation, it cannot directly serve as an epitaxial template thus considerably adding more complicity to the deposition process.

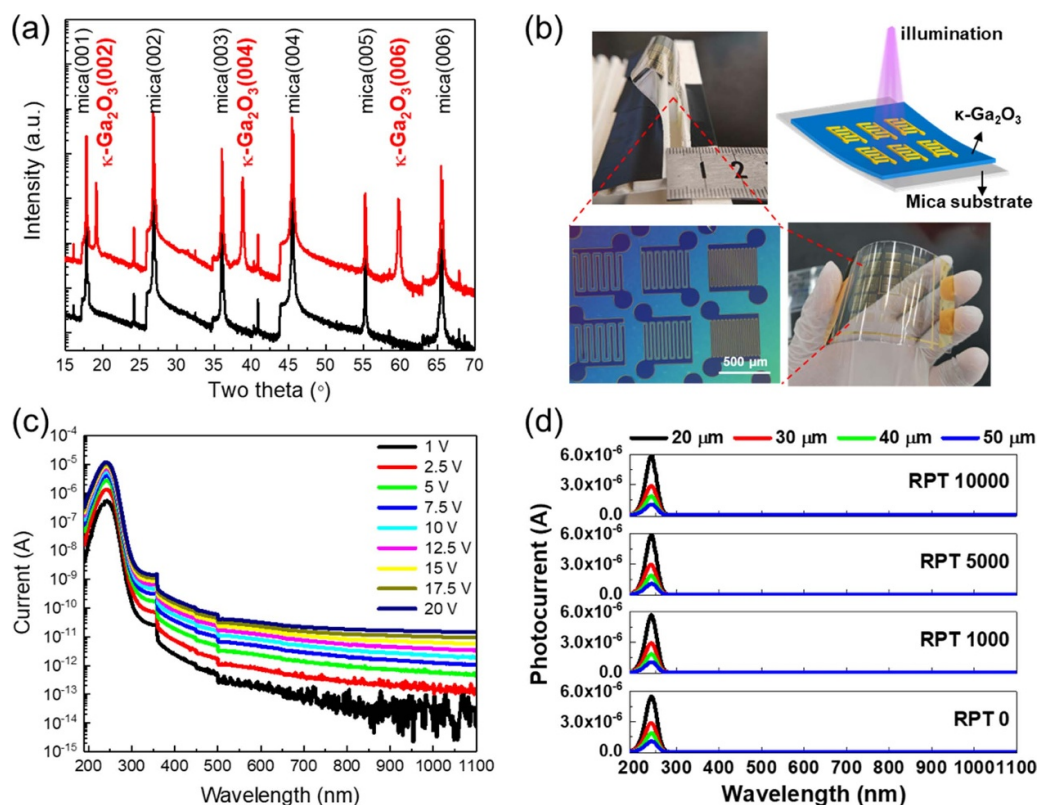


Figure 19. (a) X-ray diffraction patterns of κ -Ga₂O₃ grown on mica. (b) Fabricated flexible κ -Ga₂O₃ photodetector (PD) (1 cm × 1 cm and 5 cm × 5 cm scales) with interdigital patterns under bending. (c) Log-scale photocurrent spectrum of the PD for a 30 μm spacing for wavelengths from 190 to 1100 nm. (d) Photoresponse spectra of devices with spacing distances of 20, 30, 40, and 50 μm measured after 0, 1000, 5000, and 10000 bending cycles [130]. Copyright 2022 ACS.

7. Summary and future challenges

The application of β -Ga₂O₃ in flexible devices can pave the way for the development of wearable and portable high-performance devices, such as power electronics, solar-blind UV detectors, and memory devices. As a ceramic material, the growth of high-quality β -Ga₂O₃ thin films requires high crystallization temperature and templates with appropriate lattice constants for epitaxial growth; however, polymer substrates cannot withstand high temperatures. Accordingly, three main strategies have been developed for the fabrication of flexible β -Ga₂O₃ devices: the transfer route, *in-situ* room-temperature amorphous route, and *in-situ* high-temperature epitaxy route. Each method has advantages and limitations. In the transfer route, bulk single-crystalline β -Ga₂O₃ is first obtained using conventional techniques for growth under high-temperature conditions; then, β -Ga₂O₃ thin films are exfoliated from bulk materials and transferred to the flexible polymer substrates. Owing to the high crystal quality inherited from the bulk β -Ga₂O₃ material, the intrinsic changes in the photoelectric performance of flexible β -Ga₂O₃ devices caused by lattice deformation or intergranular fracture can be studied under bending conditions. However, the high crystal quality is obtained at the price of scaling and reproducibility owing to complicated manual operation. Hence, the transfer route can hardly be employed in production. To overcome complexity and irreproducibility, the straightforward route is used to

deposit Ga₂O₃ thin films on flexible substrates *in-situ*. However, the thermal stability of polymer substrates does not meet the requirements for the high-temperature growth of β -Ga₂O₃. Hence, a feasible solution is to deposit amorphous Ga₂O_x thin films at room temperature. Compared with β -Ga₂O₃, amorphous Ga₂O_x has relatively low thermal stability, and its stoichiometry is variable and highly dependent on deposition parameters. In this regard, oxygen flux and post-thermal treatment were employed to obtain high-performance amorphous Ga₂O_x. Such amorphous Ga₂O_x flexible thin films can be readily fabricated into PDs with good photoelectric performance. Moreover, compared with the complicated transfer route, the amorphous Ga₂O_x grown *in-situ* offers large-scale deposition of homogeneous Ga₂O_x thin films on which conventional photolithography patterning can be performed to create photodetection arrays. However, most applications of Ga₂O_x thin films remain limited to the photodetection area. Owing to the relatively unpredictable and unstable electrical performances of the thin films, their use in power devices is challenging. To realize the *in-situ* growth of single-crystalline β -Ga₂O₃ thin films, the primary requirements for flexible substrates include high thermal stability up to the temperature range for β -Ga₂O₃ crystallization and ideal lattice match for β -Ga₂O₃ growth. Consequently, single-crystalline Ga₂O₃ thin films were fabricated on mica and CeO₂-functionalized Hastelloy flexible substrates. As a ceramic material, single-crystalline mica sheets can simultaneously meet thermal and lattice requirements.

Hastelloy can withstand high temperatures up to 1300 °C. However, because of its polycrystalline nature, additional multiple oxide coatings are necessary to obtain its epitaxy ability. Until now, the development of such ceramic/functionalized alloy substrates is still in the early stages; hence, the produced Ga₂O₃ flexible thin films currently have limited application.

Various challenges must be overcome before the development of flexible Ga₂O₃ devices. First, the absence of solid demonstrations of p-type conductivity and the prediction that holes are self-trapped to form polarons limit the current range of Ga₂O₃ devices to unipolar conductivity [141, 142]. Hence, efforts are required to explore p-type Ga₂O₃ for wider electronic applications.

In view of the device configuration, nowadays, the aforementioned works are more limited to individual ones or arrays of the same type of device with the same functions. To fully explore the potential of Ga₂O₃ in electronic applications, the devices must be implanted on a chip in a more complicated arrangement or with multiple functions. For instance, arranging the Ga₂O₃ TFTs in series or in parallel mode can make them into AND, NAND, NOR, and OR logic gates, which can open a larger world for the flexible Ga₂O₃ devices, such as wearable processors; by utilizing similar designs, the TFTs can be integrated into DC/DC converter, which is crucial to the adaptability of the Ga₂O₃ photoelectric devices such as memory, PDs, sensors, and processors, to a variety of power-supply systems with different input voltages. Moreover, by modifying the TFT structures to a floating gate configuration, the TFTs can function as a logic memory, therefore largely shrinking the required circuit size for the potential wearable computing devices. Given the fact that for wearable and portable electronics, the size limitation is a crux for their commercial end, thus for all these devices, it is desired to integrate them in a monolithic, which can also considerably eliminate the parasitic effects and enhance the working efficiency. In this context, it triggers more tackles in the nanofabrication processes when using flexible substrates, such as the thickness inhomogeneity for the individual layers of the multi-layer stacked structure, and the defocus problem during the patterning procedures caused by the unavoidable tension of the flexible substrates. Another research trend is the integration of Ga₂O₃ with other semiconductor materials to create various heterostructures, therefore providing enhanced or multiple functions of the integrated devices, such as PDs with enhanced performances, self-powered PDs, and CMOS circuits [143–146]. However, in such a regime, the epitaxial ability of the flexible template for materials with varied lattice structures becomes a new challenge.

Besides, the tests of the aforementioned *in-situ* deposition techniques remain limited to the laboratory scale. To realize large-scale production, techniques compatible with reel-to-reel systems must be developed [147]. The establishment of a pilot production line becomes imperative to evaluate and improve the production cost and material quality.

At last, the use of wearable electronics relies heavily on power supply systems that are flexible and lightweight and

provide stable and operation-matched output voltage. However, due to the lack of stable and flexible power supply systems, conventional rigid electronics powered by rigid battery pads dominate the market [148, 149]. To advance the development of flexible electronics, the integration of such individual components is essential. The utmost challenge to confront is the feasibility of the power supply system. For instance, the solar cell is regarded as the most convenient and cost-effective power supply system for wearable electronics [150]. However, the light harvesting of solar cells can fluctuate dramatically depending on weather conditions, thereby hindering the allocation of stable and adjustable input voltage to electronic devices. In this regard, it is obligatory to embed a flexible circuit board to regulate and tune the output voltage in line with specific requirements. Tackling these issues and developing other electronic components (i.e. solar cells and circuit boards) can enable the development of flexible Ga₂O₃ thin film-based integrated electronics.

Data availability statement

No new data were created or analysed in this study.

Acknowledgments

The authors would like to acknowledge the support of KAUST Baseline BAS/1/1664-01-01, KAUST Competitive Research Grant URF/1/3437-01-01, URF/1/3771-01-01, and GCC Research Council REP/1/3189-01-01.

ORCID iDs

Xiao Tang  <https://orcid.org/0000-0002-0138-7206>

Xiaohang Li  <https://orcid.org/0000-0002-4434-365X>

References

- [1] Pearton S J, Yang J, Cary P H, Ren F, Kim J, Tadjer M J and Mastro M A 2018 *Appl. Phys. Rev.* **5** 011301
- [2] Higashiwaki H 2022 *AAPPS Bull.* **32** 3
- [3] Guo D, Guo Q, Chen Z, Wu Z, Li P and Tang W 2019 *Mater. Today Phys.* **11** 100157
- [4] Liu Z, Li P, Zhi Y, Wang X, Chu X and Tang W 2019 *Chin. Phys. B* **28** 017105
- [5] Zhou H, Zhang J, Zhang C, Feng Q, Zhao S, Ma P and Hao Y 2019 *J. Semiconduct.* **40** 011803
- [6] Sheoran H, Kumar V and Singh R 2022 *ACS Appl. Electron. Mater.* **4** 2589
- [7] Chen X, Ren F, Gu S and Ye J 2019 *Photon. Res.* **7** 381
- [8] Tak B R, Kumar S, Kapoor A K, Wang D, Li X, Sun H and Singh R 2021 *J. Appl. Phys.* **54** 453002
- [9] Wang Y, Su J, Lin Z, Zhang J, Chang J and Hao Y 2022 *J. Mater. Chem. C* **10** 13395
- [10] Mandal P, Roy S and Singh U P 2022 *Opt. Quantum Electron.* **54** 8
- [11] Bae J-H, Hyoung W-K, Kang I-H and Kim J 2019 *RSC Adv.* **9** 9678

- [12] Mastro M A, Kuramata A, Calkins J, Kim J, Ren F and Pearton S J 2017 *ECS J. Solid State Sci. Technol.* **6** 356
- [13] Yadava N, Mani S and Chauhan R K 2020 *J. Semiconduct.* **41** 122803
- [14] Su J, Guo R, Lin Z, Zhang S, Zhang J, Chang J and Hao Y 2018 *J. Phys. Chem. C* **122** 24592
- [15] Zhang H, Tang H L, He N-T, Zhu Z-C, Chen J-W, Liu B and Xu J 2020 *Chin. Phys. B* **29** 087201
- [16] Bae J-B, Kim H-W, Kang I-H, Yang G and Kim J 2020 *Appl. Phys. Lett.* **112** 122102
- [17] Son J, Kwon Y, Kim J and Kim J 2018 *ECS J. Solid State Sci. Technol.* **7** Q148
- [18] Fang P, Rao C, Liao C, Chen S, Wu Z, Lu X, Chen Z, Wang G, Liang J and Pei Y 2022 *Semicond. Sci. Technol.* **37** 115007
- [19] Wenxiu Gao W, Zhu Y, Wang Y, Yuan G and Liu J-M 2020 *J. Mater. Sci.* **6** 1
- [20] Sun Y and Rogers J A 2007 *Adv. Mater.* **19** 1897
- [21] Gao W, Ota H, Kiriya D, Takei K and Javey A 2019 *Acc. Chem. Res.* **52** 523
- [22] Gates B D 2009 *Science* **323** 1566
- [23] Wang L, Chen D, Jiang K and Shen G 2017 *Chem. Soc. Rev.* **46** 6764
- [24] Robert J H 2001 *Nature* **412** 489
- [25] Ling H, Liu S, Zheng Z and Yan F 2018 *Small Methods* **2** 1800070
- [26] Lewis J 2006 *Mater. Today* **9** 38
- [27] Chen Y, Zhang Y, Liang Z, Cao Y, Han Z and Feng X 2020 *npj Flex. Electron.* **4** 2
- [28] Liu Z, Jing Xu J, Chen D and Shen G 2015 *Chem. Soc. Rev.* **44** 161
- [29] Chambers S A 2000 *Surf. Sci. Rep.* **39** 105
- [30] Luryi S and Suhir E 1986 *Appl. Phys. Lett.* **49** 21
- [31] Headley T J and Loehman R E 1984 *J. Am. Ceram. Soc.* **67** 620
- [32] Playford H Y, Hannon A C, Barney E R and Walton R I 2013 *Chemistry A* **19** 2803
- [33] Yoshioka S, Hayashi H, Kuwabara A, Oba F, Matsunaga K and Tanaka I 2007 *J. Phys.: Condens. Matter* **19** 346211
- [34] Logothetidis S 2008 *Mater. Sci. Eng. B* **152** 96
- [35] Tang X *et al* 2022 *ACS Appl. Mater. Interfaces* **14** 1304
- [36] Lu Y *et al* 2022 *ACS Appl. Mater. Interfaces* **14** 47922
- [37] Huang Y, Gao A, Guo D, Lu X, Zhang X, Huang Y, Yu J, Li S, Li P and Tang W 2020 *J. Mater. Chem. C* **8** 536
- [38] Geller S 1960 *J. Chem. Phys.* **33** 676
- [39] Wang J, H *et al* 2020 *IEEE Electron Device Lett.* **41** 1052
- [40] Kaneko K, Uno K, Jinno R and Fujita S 2022 *J. Appl. Phys.* **131** 090902
- [41] Heinemann M D, Berry J, Teeter G, Unold T, D and Ginley D 2016 *Appl. Phys. Lett.* **108** 022107
- [42] Sui Y, Liang H, Chen Q, Huo W, Du X and Mei Z 2022 *ACS Appl. Mater. Interfaces* **12** 8929
- [43] Nagarajan L, Souza R A D, Samuelis D, Valov I, Börger A, Janek J, Becker K-D, Schmidt P C and Manfred Martin M 2008 *Nat. Mater.* **7** 391
- [44] Kawaharamura T, Dang G T and Furuta M 2012 *Jpn. J. Appl. Phys.* **51** 040207
- [45] Uno K, Ohta M and Tanaka I 2020 *Appl. Phys. Lett.* **117** 052106
- [46] Akaiwa K and Fujita S 2020 *Jpn. J. Appl. Phys.* **51** 070203
- [47] Tang X, Li K-H, Liao C-H, Vasquez J M T, Wang C, Xiao N and Li X 2022 *J. Eur. Ceram. Soc.* **42** 175
- [48] Nikolaev V I, Pechnikov A I, Nikolaev V V, Scheglov M P, Chikiryaka A V, Stepanov S I, Medvedev O S, Shapenkov S V, Ubyivovk E V and Vyvenko O F 2019 *J. Phys.: Conf. Ser.* **1400** 055049
- [49] Muruganandham M, Amutha R, Wahed M S M A, Ahmmad B, Kuroda Y, Suri R P S, Wu J J and Sillanpää M E T 2012 *J. Phys. Chem. C* **116** 44
- [50] Hajnal Z, Mirao J, Kiss G, Raeti F, P, Deak P, Herndon R C and Kuperberg J M 1999 *J. Appl. Phys.* **86** 3792
- [51] Kaneko K, Nomura T, Takeya I and Fujita S 2009 *Appl. Phys. Express* **2** 075501
- [52] Oshima T, Matsuyama K, Yoshimatsua K and Ohtomoab A 2015 *J. Cryst. Growth* **421** 23
- [53] Cho S-B and Mishra R 2018 *Appl. Phys. Lett.* **112** 16210
- [54] Kracht M *et al* 2017 *Phys. Rev. Appl.* **8** 054002
- [55] Nikolaev V I, Stepanov S I, Pechnikov A I, Shapenkov S V, Scheglov M P, Chikiryaka A V and Vyvenko O F 2020 *ECS J. Solid State Sci. Technol.* **9** 045014
- [56] Hsu Y-H, Wu W-Y, Lin K-L, Chen Y-H, Lin Y-H, Liu P-L, Hsiao C-L and Horng R-H 2022 *Cryst. Growth Des.* **22** 1837
- [57] Qian L-X, Zhang H F, Lai P T, Wu Z-H and Liu X-Z 2017 *Opt. Mater. Express* **7** 3643
- [58] Xu J, Zheng W and Huang F 2019 *J. Mater. Chem. C* **7** 8753
- [59] Kokubun Y, Miura K, Endo F and Nakagomi S 2007 *Appl. Phys. Lett.* **90** 031912
- [60] Blumenschein N, Paskova T and Muth J F 2019 *Phys. Status Solidi a* **216** 1900098
- [61] Meng L, Feng Z, Bhuiyan A F M A U and Zhao H 2022 *Cryst. Growth Des.* **22** 3896
- [62] Wang Y, Li S, Cao J, Jiang Y, Zhang Y, Tang W and Wu Z 2022 *Mater. Des.* **221** 110917
- [63] Wang Y *et al* 2021 *ACS Nano* **15** 16654
- [64] Tien T-C, Wu J-S, Hsieh T-E and Wu H-J 2022 *Coatings* **12** 1217
- [65] Iijima Y, Kakimoto K, Kimura M, Takeda K and Saitoh T 2001 *IEEE Trans. Appl. Supercond.* **11** 2816
- [66] Saki Z, Byranvand M M, Taghavinia N, Kedia M and Saliba M 2021 *Energy Environ. Sci.* **14** 5690
- [67] Seidelmann L J, Bradley J W, Ratova M, Hewitt J, Moffat J and Kelly P 2017 *Appl. Sci.* **7** 337
- [68] MacDonald W A, Looney M K, MacKerron D, Eveson R, Adam R, Hashimoto K and Rakos K 2007 *J. Soc. Inf. Disp.* **15** 1075
- [69] Huang S, Li M, Garner S M, Li M-J and Chen K P 2015 *Opt. Express* **23** 22532
- [70] Nejand B A, Nazari P, Gharibzadeh S, Ahmadi V and Moshaii A 2017 *Chem. Commun.* **53** 747
- [71] Nasiri M and Rozati S M 2018 *Mater. Sci. Semicond. Process.* **81** 38
- [72] Wong W S and Salleo A 2009 *Flexible Electronics: Materials and Applications* (New York: Springer)
- [73] Chen C-K, Lin Y-C, Miyane S, Ando S, Ueda M and Chen W-C 2020 *ACS Appl. Polym. Mater.* **2** 3422
- [74] Nair S S, Forsythe J and Winther-Jensen B 2015 *RSC Adv.* **5** 90881
- [75] Cesarini M, Brigante B, Caironi M and Natali D 2018 *ACS Appl. Mater. Interfaces* **10** 32380
- [76] Gueye M N, Carella A, Demadrille R and Simonato J-P 2017 *ACS Appl. Mater. Interfaces* **9** 27250
- [77] Xiang L, Zhang H, Hu Y and Peng L-M 2018 *J. Mater. Chem. C* **6** 7714
- [78] Zhang W, Yang H, Li L, Lin S, Ji P, Hu C, Zhang D and Xi Y 2020 *Nanotechnology* **31** 385401
- [79] El-Atab N and Hussain M M 2020 *MRS Energy Sustain. Rev.* **7** e19
- [80] Kim C-D, Yoo J-S, Lee J-K, Yoon S-Y, Yong In Park Y-I, Kang I-B and Chung I-J 2009 2009 *Flexible Electronics & Displays Conf. and Exhibition* p 1
- [81] Chen T C, Yue G L, Kai W, Shiue R K and Tsay L W 2022 *Materials* **15** 2483
- [82] Pouladi S *et al* 2019 *Prog. Photovolt.: Res. Appl.* **27** 30–36
- [83] Liu Y, Li Y, El-hady A M, Zhao C, Du J, Liu Y and Fu Y 2015 *Sens. Actuators B* **221** 230
- [84] Suo H, Gao M, Zhao Y, Zhu Y, Gao P, Wang J, Liu M, Ma L and Ji Y 2010 *IEEE Trans. Appl. Supercond.* **20** 1569

- [85] Zhao Y, Suo H, Zhu Y, Liu M, He D, Ye S, Ma L, Fan R, Ji Y and Zhou M 2008 *Supercond. Sci. Technol.* **21** 075003
- [86] Ma L, Suo H L, Zhao Y, Wulff A C, Liang Y R and Grivel J-C 2014 *IEEE Trans. Appl. Supercond.* **3** 1558
- [87] Zhao Y *et al* 2019 *Supercond. Sci. Technol.* **32** 044004
- [88] Khan M Z, Rivasto E, Wu Y, Zhao Y, Chen C, Zhu J, Palonen H, Tikkanen J, Huhtinen H and Paturi P 2020 *J. Phys.: Conf. Ser.* **1559** 012037
- [89] Dutta P *et al* 2014 *Appl. Phys. Lett.* **105** 092104
- [90] Peres M *et al* 2019 *ECS J. Solid State Sci. Technol.* **8** Q3235
- [91] Wang X, Wu Z, Cui W, Zhi Y, Li Z, Li P, Dao-You Guo D and Tang W 2019 *Chin. Phys. B* **28** 017305
- [92] Zhang D, Chen H, He W, Hong Z, Lu Q, Guo L, Liu T, Liu X and Hao Y 2021 *Superlattices Microstruct.* **160** 107078
- [93] Swinnich E, Hasan M N, Zeng K, Dove Y, Singiseti U, Mazumder B and Seo J-H 2019 *Adv. Electron. Mater.* **5** 1800714
- [94] Li X-X, Zeng G, Li Y-C, Zhang H, Ji Z-G, Yang Y-G, Luo M, Hu W-D, Zhang D W and Lu H-L 2022 *npj Flex. Electron.* **6** 47
- [95] Hasan M N, Lai J, Swinnich E, Zheng Y, Baboukani B S, Nalam P C and Seo J-H 2021 *Adv. Electron. Mater.* **7** 2000763
- [96] Lai J, Hasan M N, Swinnich E, Tang Z, Shin S-H, Kim M, Zhang P and Seo J-H 2020 *J. Mater. Chem. C* **8** 14732
- [97] Mitdank R, Dusari S, Bülow C, Albrecht M, Galazka Z and Fischer S F 2014 *Phys. Status Solidi a* **211** 543
- [98] Galazka Z 2022 *J. Appl. Phys.* **131** 031103
- [99] Ullah S, Yang X, Ta Q, Hasan H, Bachmatiuk M, Tokarska A, Trzebiecka K, Fu B and Rummeli M H 2021 *Nano Res.* **14** 3756
- [100] Zhu W, Yogeesh M N, Yang S, Aldave S H, Kim J-S, Sonde S, Tao L, Lu N and Akinwande D 2015 *Nano Lett.* **15** 1883
- [101] Chun J, Hwang Y, Choi Y-S, Jeong T, Baek J-H, Ko H and Park S-J 2012 *IEEE Photonics Technol. Lett.* **24** 2115
- [102] Sharma M, Singh A and Singh R 2020 *ACS Appl. Nano Mater.* **3** 4445
- [103] Liu Z *et al* 2020 *J. Phys. D: Appl. Phys.* **53** 085105
- [104] Ju H, Liu J, Wang B, Tao X, Ma Y and Xu S 2013 *Ceram. Int.* **39** 857
- [105] Tang X, Li K-H, Liao C-H, Zheng D, Liu C, Lin R, Xiao N, Krishna S, Tauboda J and Li X 2021 *J. Mater. Chem. C* **9** 15868
- [106] Wakabayashi R, Yoshimatsu K, Hattori M and Ohtomo A 2017 *Appl. Phys. Lett.* **111** 162101
- [107] Nishinaka H, Tahara D and Yoshimoto M 2016 *Jpn. J. Appl. Phys.* **55** 1202BC
- [108] Kaneko K, Ito H, Lee S-D and Fujita S 2013 *Phys. Status Solidi c* **10** 1596
- [109] Salles P, Caño I, Guzman R, Dore C, Mihi A, Zhou W and Coll M 2021 *Adv. Mater. Interfaces* **8** 2001643
- [110] Liang H, Cui S, Su R, Guan P, He Y, Yang L, Chen L, Zhang Y, Mei Z and Du X 2019 *ACS Photonics* **6** 351
- [111] Cui S, Mei Z, Zhang Y, Liang H and Du X 2017 *Adv. Opt. Mater.* **5** 1700454
- [112] Wang T, Liang H, Han Z, Sui Y and Mei Z 2021 *Adv. Mater. Technol.* **6** 2000945
- [113] Yang Y, Liu W, Huang T, Qiu M, Zhang R, Yang W, He J, Chen X and Ning Dai N 2021 *ACS Appl. Mater. Interfaces* **13** 41802
- [114] Wang H, Ma J, Cong L, Zhou H, Li P, Fei L, Li B, Xu H and Liu Y 2021 *Mater. Today Phys.* **20** 100464
- [115] Kumar N, Patel M, Kim J, Jeong C and Wong C-P 2022 *Appl. Mater. Today* **29** 101620
- [116] Li Z *et al* 2019 *IEEE Photon. J.* **11** 6803709
- [117] Gan K-J, Liu P-T, Chien T-C, Ruan D B and Sze S M 2019 *Sci. Rep.* **9** 14141
- [118] Chen Y, Lu Y, Liao M, Tian Y, Liu Q, Gao C, Yang X and Shan C 2019 *Adv. Funct. Mater.* **29** 1906040
- [119] Chen Y, Yang X, Zhang Y, Chen X, Sun J, Xu Z, Li K, Dong L and Shan C 2022 *Nano Res.* **15** 3711
- [120] Bhalerao S R, Lupo D and Berger P R 2021 *2021 IEEE Int. Flexible Electronics Technology Conf. (IFETC)* p 0032
- [121] Tang X, Zhao Y, Wu W and Grivel J-C 2015 *J. Mater. Sci. Mater. Electron.* **26** 1806
- [122] Tang X, Zhao Y and Grivel J-C 2013 *Ceram. Int.* **39** 7735
- [123] Tang X, He D, Zhao Y and Grivel J-C 2013 *IEEE Trans. Appl. Supercond.* **24** 74
- [124] Driessche I V *et al* 2012 *Supercond. Sci. Technol.* **25** 065017
- [125] Zhao Y, Konstantopoulou K, Wulff A C, Tang X, Tian T, Suo H, Pastor J Y and Grivel J-C 2012 *IEEE Trans. Appl. Supercond.* **23** 6600104
- [126] Zhang Z *et al* 2017 *Adv. Mater.* **29** 1702359
- [127] Xu X, Liu W, Li Y, Wang Y, Yuan Q, Chen J, Ma R, Xiang F and Wang H 2018 *J. Mater. Chem. A* **6** 173
- [128] Ren W, Huang W, Zhu H, Wang D, Zhu L-G and Shi Q 2021 *Vacuum* **192** 110407
- [129] Liu C-F, Tang X-G, Wang L-Q, Tang H, Jiang Y-P, Liu Q-X, Li W-H and Tang Z-H 2019 *Nanomaterials* **9** 1124
- [130] Wen X, Lu Z, Valdman L, Wang G-C and Washington M 2020 *ACS Appl. Mater. Interfaces* **12** 35222
- [131] Li Y, Liu X, Wen D, Lv K, Zhou G, Zhao Y, Xu C and Wang J 2020 *Acta Crystallogr. B* **76** 233
- [132] Li Y, Feng J, Zhang J, He B, Wu Y, Zhao Y, Xu C and Wang J 2021 *Appl. Surf. Sci.* **556** 149798
- [133] Kim N I, Chen J, Wang W, Moradnia M, Pouladi S, Kwon M-K, Kim J-Y, Li X and Ryou J-H 2021 *Adv. Funct. Mater.* **31** 2008242
- [134] Li Y, Feng J, Wang Y, He B, Zhao Y, Xu C and Wang J 2021 *Appl. Surf. Sci.* **568** 150925
- [135] Li Y, Feng J, Zhao Y, Wang J and Xu C 2022 *Appl. Surf. Sci.* **599** 153969
- [136] Shervin S *et al* 2022 *Sol. Energy Mater. Sol. Cells* **243** 111791
- [137] Tak B R, Gupta V, Kapoor A-K, Chu Y-H and Singh R 2019 *ACS Appl. Electron. Mater.* **1** 2463
- [138] Sui Y, Liang H, Huo W, Wang Y and Mei Z 2020 *J. Phys. D: Appl. Phys.* **53** 504001
- [139] Tak B-R, Yang M-M, Lai Y, Chu Y-H, Alexe M and Rajendra Singh R 2020 *Sci. Rep.* **10** 16098
- [140] Lu Y, Krishna S, Tang X, Babatrain W, Hassine M-B, Liao C-H, Xiao N, Liu Z and Li X 2022 *ACS Appl. Mater. Interfaces* **14** 34844
- [141] Zeman C J, Kielar S M, Jones L O, Mosquera M A and Schatz G C 2021 *J. Alloys Compd.* **877** 160227
- [142] Kyrtos A, Matsubara M and Bellotti E 2018 *Appl. Phys. Lett.* **112** 032108
- [143] Wang Y, Yang Z, Li H, Li S, Zhi Y, Yan Z, Huang X, Wei X, Tang W and Wu Z 2020 *ACS Appl. Mater. Interfaces* **12** 47714
- [144] Wang Y H *et al* 2021 *ACS Photonics* **8** 2256
- [145] Chen W-H, Ma C-H, Hsieh S-H, Lai Y-H, Kuo Y-C, Chen C-H, Chang S-P, Chang S-J, Horng R-H and Chu Y-H 2022 *ACS Appl. Electron. Mater.* **4** 3099
- [146] Moon S, Bae J and Kim J 2021 *Meet. Abstr.* **MA2021-02** 1910
- [147] Blankenburg L, Schultheis K, Schache H, Sensfuss S and Schrödner M 2009 *Sol. Energy Mater. Sol. Cells* **93** 476
- [148] Kong L, Tang C, Peng H-J, Huang J-Q and Zhang Q 2020 *SmartMat* **1** e1007
- [149] Tao T, Lu S and Chen Y 2018 *Adv. Mater. Technol.* **3** 1700375
- [150] Hashemi S A, Ramakrishna S and Aberle A G 2020 *Energy Environ. Sci.* **13** 685